A thermo-kinetic investigation on the thermal degradation of polyvinyl chloride in the presence of magnetite and hematite

Sanad Altarawneh[1],* Mohammad Al-Harahsheh[2], Adam Buttress[1], Chris Dodds[1], Sam Kingman[1]

*corresponding author: sanad.altarawneh@nottingham.ac.uk

[1] Faculty of Engineering, University of Nottingham, Nottingham, NG7 2RD, UK

[2] Chemical Engineering Department, Jordan University of Science and Technology, Irbid, 22110, Jordan

Abstract

Electric arc furnace dust (EAFD) which is accumulated in large amounts world-wide contains hematite (Fe_2O_3) and significant quantities of magnetite (Fe_3O_4). Waste polyvinyl chloride (PVC) also poses a great environmental threat aside to accumulated EAFD. Both of these wastes have shown a great potential for their co-thermal treatment for metal extraction, thus minimising their environmental footprint. Herein, an investigation on the thermal degradation behaviour, reaction products, thermodynamics and the decomposition kinetics of PVC and its stoichiometric mixtures with Fe_3O_4 and Fe_2O_3 was conducted using non-isothermal thermogravimetric scans. The kinetic data suggests a significant increase in the average activation energy of PVC de-hydrochlorination from 122.6 ± 24.2 kJ/mol (pure PVC) to 177.0 ± 28.0 and 199.0 ± 77.0 kJ/mol when stoichiometric quantities of Fe_3O_4 and Fe_2O_3 were mixed with PVC. The inhibiting effect of both Fe_3O_4 and Fe_2O_3 on the degradation of PVC might be assigned to the capturing of emitted gaseous HCl which is known for its catalytic effect. This result suggests that EAFDs containing both Fe_3O_4 (in large amounts) and Fe_2O_3 can have an inhibiting effect on the de-hydrochlorination of PVC resulting in longer processing times or the requirement of higher processing temperatures for achieving reasonable reaction rates.

Keywords: PVC; Fe_3O_4; Fe_2O_3; pyrolysis; iron oxide; non-isothermal kinetics

1. Introduction

Economic development and advancement is accompanied by a rise in the rate of waste generation [1]. Among a wide array of different industries, steel manufacturing can be considered as one of the largest industrial sectors in terms of production rate. The global annual crude steel production was 189 million tons in 1950 which increased to 850 and 1809 million tons in 2000 and 2018, respectively [2]. Electric arc furnaces (EAFs) accounted for 28% of the total steel production in 2018 [2]. This large production rate from EAFs is accompanied by harmful emissions in the form of small particle size dust which is referred to as electric arc furnace dust (EAFD). The overall hazard associated with EAFD lies in its large production rate (1–2% of EAF steel charge) [3], the presence of toxic heavy metals such as Cd and Pb [3], and the absence of a sustainable and an environmentally benign recycling route of the material.

Parallel to accumulated EAFD, there has been a significant increase in the generation rate of plastic wastes due to its extensive use in all life applications [4]. Among thermoplastics, Polyvinyl Chloride (PVC) is considered one of the most commonly used [5]. A simulation study performed by Zhou et al. [6] suggests that in China alone, the accumulated PVC waste will reach up to 600 million tons by the end of year 2050. The disposal of this waste has been the concern of many environmental engineers. Conventionally, landfilling and incineration of PVC are the most prevalent routes for disposal. Due to the stable nature of PVC [7], the former approach can result in the indefinite accumulation of PVC in landfills. The latter, on the other hand, results in the formation of hazardous emissions such as hydrogen chloride (HCl) and chlorinated hydrocarbons (dioxins) [8-12]. The adoption of an incineration approach requires finding a sustainable solution to the emissions that accompany decomposing PVC. This can involve using resistive material for the construction of the handling equipment, or the co-thermal treatment of PVC with other materials that can act as emission fixators [9, 12-14]. EAFD has been identified as an excellent candidate for the fixation of the harmful emissions

evolved from decomposing PVC [4, 10-13]. Lee and Song [13], confirmed the formation of zinc, lead, and cadmium chlorides upon thermal treatment with PVC with recovery percentages up to 96.2, 97.4 and 98.8% respectively. A series of papers published by Al-Harahsheh et al. [10-12, 14, 15], tackled the metal extraction, kinetics, and thermodynamics aspects of the co-thermal treatment of PVC with EAFD. The limitation of these studies is that they were unable to elucidate the individual contribution of each metal oxide in EAFD to the fixation of emissions as well as their effect on the kinetics of PVC degradation. Knowledge of the individual kinetic effect of each metal oxide phase is important. This is because the chemistry of EAFD can vary greatly from one site to another and from one country to another. Thus, establishing a kinetic database for the effect of each metal oxide present in EAFD on the kinetics of PVC degradation helps in making kinetic predictions for PVC decomposition mixed with EAFD from different sources with different chemistries based on their mineralogical composition.

In this study, we present a systematic non-isothermal kinetic study of the thermal de-hydrochlorination of PVC mixed with stoichiometric amounts of Fe_3O_4 and Fe_2O_3; the former is present in EAFD at high concentrations. The thermal scans were generated at different heating rates which allows the calculation of the apparent activation energy, the apparent frequency factor, and the apparent reaction model associated with the de-hydrochlorination using model free methods. A detailed identification of the solid pyrolysis products of Fe_3O_4-PVC and Fe_2O_3-PVC mixtures at different temperatures was undertaken using different solid analytical techniques.

2. Materials and method

2.1. Thermogravimetric analysis and Differential scanning calorimetry

Fe_3O_4 and PVC powders were obtained from Sigma-Aldrich, while Fe_2O_3 was obtained from Fisher scientific. Fe_3O_4 and Fe_2O_3 powders had purities of 99.99% and 99.999%, respectively. Iron oxide-PVC mixtures were prepared based on the stoichiometric amount of HCl in the PVC monomer to fully chlorinate Fe_3O_4 and Fe_2O_3 into their corresponding chloride forms ($FeCl_2$ and $FeCl_3$ for Fe_3O_4 and $FeCl_3$ for Fe_2O_3). Hence, mixtures of 31.6 and 29.9 wt% of Fe_3O_4 and Fe_2O_3 with PVC were prepared. The instrument used for the simultaneous TGA/DSC analysis was a SDT Q600. Before the analysis, an experiment with an empty sample holder (ceramic crucible) was performed to produce a baseline for the heat flow signal. Accurate amounts (10.7 ± 0.39 mg (Fe_3O_4-PVC) and 10.3 ± 0.49 mg (Fe_2O_3-PVC)) were loaded into the ceramic crucibles and the thermal analysis was performed under a nitrogen flow of 100 mL/min. Different heating rates of 10, 30 and 50 K/min for PVC and Fe_3O_4-PVC were used. For Fe_2O_3-PVC, however, heating rates of 5, 10, and 30 K/min were used. This is because the 50 K/min accentuated the effect of a certain parallel reaction resulting in a larger mass loss at 50 K/min thus preventing the usage of model free kinetic approach. The temperature range used in the analysis was 25 to 900 °C.

2.2. Pyrolysis of iron oxides-PVC mixtures

A sample of 0.32 ± 0.0075 g of each mixture was loaded in a 4 mm diameter quartz tube. The powder was pre-purged with nitrogen (purity: 99.9992%) for at least 15 minutes to allow the formation of a nitrogen blanket around the reactants, after which the flow was held at ~5 mL/min. The pyrolysis temperatures were 400, 550, 650, and 850 °C for Fe_3O_4-PVC and 400, 600, and 850 °C for Fe_2O_3-PVC. The different temperature choice for each mixture was made because of their distinct TGA profiles such that each temperature resembles a plateau after

every stage. The reactants were loaded into the furnace and were held at the desired temperature for 30 minutes. The pyrolysis products were taken out of the reactor, purged with nitrogen, and stored in a desiccator for further analysis.

2.3. Mineralogy characterisation

The pyrolysis residues were characterised using X-Ray Diffraction (XRD). Due to the hygroscopic nature of the generated powder, the sample was covered with plastic tape during the analysis to prevent it from being exposed to the ambient atmosphere. The analysis was conducted on a Bruker D8 Advance XRD machine. The mineralogy of the generated phases were studied in the 2θ range of 5 – 90° at a step size of 0.02° with a scan time of 1.7 sec/step. The radiation source was Cu kα and the X-ray tube was operated at a current and a voltage of 40 mA and 40 kV, respectively.

2.4. Morphology and chemistry characterisation

The pyrolysis residues were characterised for morphology and chemistry using FEI Quanta600 MLA scanning electron microscope (SEM) coupled with energy dispersive spectroscopy (EDS). A small amount of the pyrolysis residue was sprinkled on a stub covered with a carbon adhesive layer. Powders on stubs were coated with a 8.2 ± 1.4 nm layer of carbon to enhance the electrical conductivity during the analysis to prevent electron charging. The operating conditions of the SEM instrument were: spot size of 5.00 and an accelerating voltage of 15.0 kV.

2.5. Particle size analysis

Since the particle size can have an impact on the contact surface area between reactants, the particle sizes of the materials used in this work were measured. The instrument used for the analysis was the Beckman Coulter LS13320MW laser diffraction analyser with an Aqueous

Liquid Module (ALM). The particle size was measured for the as received materials used in this work (PVC, Fe_3O_4, and Fe_2O_3) and are reported in Table 2.

2.6. Thermodynamics simulation

Due to the presence of a large number of possible reduction reactions, the interpretation of the kinetic data becomes easier with the presence of thermodynamics data. FACTSAGE software package was used to calculate the change in the Gibbs free energy associated with the relevant reactions during the course of PVC degradation in the presence of Fe_3O_4 and Fe_2O_3 in the temperature window 20 – 1000 °C. Based on this data, one can know if a certain reaction lies majorly forward or backwards (i.e., its equilibrium status).

3. Non-isothermal kinetics and modelling

3.1. Kinetic rate equation

In non-isothermal kinetics, the mass of the sample is monitored while being heated at a fixed heating rate β. The loss/gain in mass is represented by the conversion (α) which is given by:

$$\alpha = \frac{M_o - M}{M_o - M_f} \quad (1)$$

Where M_o is the initial mass%, M_f is the final mass%, and M is the mass% at any time t.

The rate (r_A) of mass loss/gain is thus represented by the derivative of the conversion with respect to time $\left(\frac{d\alpha}{dt}\right)$ which is given as the product of the temperature dependent rate constant $k(T)$ and the temperature independent conversion function $f(\alpha)$ [16]:

$$r_A = \frac{d\alpha}{dt} = k(T).f(\alpha) \quad (2)$$

The rate constant dependency on temperature can be described by the Arrhenius function:

$$k(T) = Aexp\left(\frac{-E}{RT}\right) \quad (3)$$

In which, A is the frequency factor in min^{-1}, E is the activation energy J/mol, and R is the universal gas constant (8.314 J/mol .K).

The general expression of the conversion function is given by the empirical equation introduced by Šesták and Berggren [17]:

$$f(\alpha) = \alpha^m(1 - \alpha)^n[-\ln(1-\alpha)]^p \quad (4)$$

Such that, m, n, and p, are empirically obtained exponents, and different combinations of them yield different reaction models [18]. By substituting the values of $f(\alpha)$, $k(T)$, and the heating rate $\beta = \frac{dT}{dt}$ in Equation 2, we obtain the following equation:

$$\frac{r_A}{\beta} = \frac{d\alpha}{dT} = \frac{A}{\beta}exp\left(\frac{-E}{RT}\right).(\alpha^m(1 - \alpha)^n[-\ln(1-\alpha)]^p) \quad (5)$$

Equation 5 shows the derivative form of the rate equation. By rearranging and integrating both sides, we reach at the integral form:

$$g(\alpha) = \int_0^\alpha \frac{d\alpha}{\alpha^m(1-\alpha)^n[-\ln(1-\alpha)]^p} = \int_{T_o}^{T} \frac{A}{\beta}exp\left(\frac{-E}{RT}\right)dT \quad (6)$$

The most reliable techniques that are able to track the variation in the apparent activation energy and the frequency factor with conversion are the model free kinetic methods [19, 20].

3.2. Calculation of the activation energy

3.2.1. Model free kinetic methods

Model free methods rely on the principle that at a fixed conversion level, the rate of degradation is a function of temperature only [18]. This can be visualised by taking the logarithmic derivative of Equation 2 with respect to the reciprocal of temperature at a constant conversion [18]:

$$\left[\frac{\partial \ln\left(\frac{d\alpha}{dt}\right)}{\partial T^{-1}}\right]_{\alpha} = \left[\frac{\partial \ln f(\alpha)}{\partial T^{-1}}\right]_{\alpha} + \left[\frac{\partial ln(k(T))}{\partial T^{-1}}\right]_{\alpha} = 0 + \frac{-E_{\alpha}}{R} \quad (7)$$

Equation 7 tells us that knowledge of the iso-conversional activation energy can be achieved without needing to assume any reaction model, hence comes the name model-free [18].

3.2.1.1. Differential model free method

The Friedman method [19] utilises the differential form (Equation 5) of the rate equation with slight adjustment to the following form:

$$ln\left(\beta \frac{d\alpha}{dT}\right)_{\alpha,i} = ln\left(\frac{d\alpha}{dt}\right)_{\alpha,i} = ln\big(Af(\alpha)\big) - \frac{E_{\alpha}}{RT_{\alpha,i}} \quad (8)$$

At a specific conversion at a certain heating rate, specific values of $ln\left(\frac{d\alpha}{dt}\right)$ and $\frac{1}{T}$ are obtained. Hence, a plot of $ln\left(\frac{d\alpha}{dt}\right)$ against $\frac{1}{T}$ at a minimum of three different heating rates, yields a straight line with a slope of $\frac{-E_{\alpha}}{R}$ from which the apparent activation energy is calculated.

3.2.1.2. Integral model free method

Instead of performing the integration on the conversion function from 0 to α, performing it on small segments between α_0 and α_1 (such that $\alpha_1 - \alpha_0 = 0.02$) allows numerical integrations to be performed accurately. A numerical integration method was applied by Ortega [20] leading to the following final equation:

$$ln\left(\frac{\beta_i}{T_1 - T_0}\right) = ln\left(\frac{A}{F(\alpha_1) - F(\alpha_0)}\right) - \frac{E_{\alpha}}{RT_{avg}} \quad (9)$$

Such that $F(\alpha)$ is the indefinite anti-derivative of $\frac{1}{f(\alpha)}$, and T_o and T_1 are the temperatures corresponding to conversions α_0 and α_1, respectively. T_{avg} is the average temperature and is given as follows:

$$T_{avg} = \frac{T_1 + T_0}{2} \quad (10)$$

Using thermograms recorded at a minimum of three different heating rates, a plot of $ln\left(\frac{\beta_i}{T_1-T_0}\right)$ against $\frac{1}{T_{avg}}$ yields a straight line with a slope of $-\frac{E_\alpha}{R}$ from which the apparent activation energy can be calculated.

3.3. Calculation of the frequency factor using the compensation effect

This method relies on the principle that values of $ln(A)$ and E, whether they are correct or not are linearly correlated [21]. This relation can be built by fitting the experimental rate data to different reaction models $f(\alpha)$ (differential) or $g(\alpha)$ (integral). In this case, Equation 11 was used and hence the differential form $f(\alpha)$ of the reaction model was used.

$$ln\left(\frac{d\alpha}{dt}.\frac{1}{f(\alpha)}\right) = ln(A) - \frac{E}{RT} \quad (11)$$

The most common reaction models are presented in Table 1. When a set of $ln\ (A)$ is obtained against a set of E, these values are plotted against each other. The mathematical formula of the linear regression line should correspond to this equation:

$$l\,n(A)_i = aE_i + b \quad (12)$$

Such that, a and b are constants, while $l\,n(A)_i$ and E_i are each value generated using each reaction model. When the compensation chart is built, iso-conversional values of E_α obtained from the model free methods mentioned earlier can be substituted in Equation 12 to extract their corresponding iso-conversional values of $l\,n(A)_\alpha$. More elaboration on this method is presented in detail in Vyazovkin [21].

3.4. Prediction of the reaction model $f(\alpha)$

Extracting the mathematical formula of the reaction model for complex mass loss where many concurrent and sequential reactions are taking place is difficult. Since apparent activation energy and frequency factor are reported here, the reaction models reported for the de-

hydrochlorination stage with and without Fe_3O_4 and Fe_2O_3 will also be apparent ones. Rearranging the intercept $I_\alpha = ln(Af(\alpha))$ generated from the Friedman model to Equation 13 allows calculating the value of $f(\alpha)$ at each conversion level. The value of lnA_α can be substituted from those obtained from the compensation effect presented above.

$$f(\alpha) = exp\,(I_\alpha - lnA_\alpha) \quad (13)$$

The calculated $f(\alpha)$ values are then plotted against conversion with all the reaction models shown in Table 1 thus allowing tracking the change in $f(\alpha)$ with conversion. A schematic diagram showing how the $f(\alpha)$ function was predicted by combining the Friedman model and the compensation effect is presented in Figure 1.

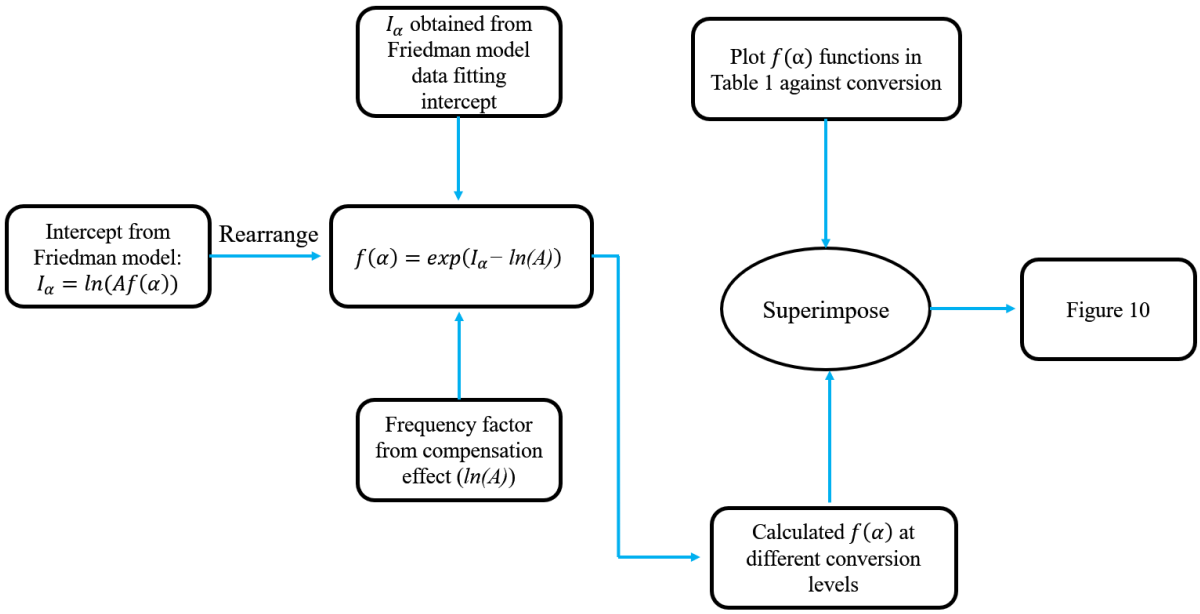

Figure 1: A schematic diagram showing how the f(α) model is predicted using a combined Friedman-compensation effect approach.

Table 1: The most important kinetic models in the differential $f(\alpha)$ and integral $g(\alpha)$ forms [22].

No.	Symbol	Kinetic model	$f(\alpha)$	$g(\alpha)$
Chemical process				
1	$F_{1/3}$	One-third order	$\frac{3}{2}(1-\alpha)^{\frac{1}{3}}$	$1-(1-\alpha)^{\frac{2}{3}}$
2	$F_{3/4}$	Three-quarters order	$4(1-\alpha)^{\frac{3}{4}}$	$1-(1-\alpha)^{\frac{1}{4}}$
3	$F_{3/2}$	One and half order	$2(1-\alpha)^{\frac{3}{2}}$	$(1-\alpha)^{\frac{-1}{2}}-1$
4	F_2	Second order	$(1-\alpha)^2$	$(1-\alpha)^{-1}-1$

5	F_3	Third order	$\frac{1}{2}(1-\alpha)^3$	$(1-\alpha)^{-2}-1$
6	F_n	n^{th} order, n > 1	$\frac{1}{n-1}(1-\alpha)^n$	$(1-\alpha)^{-n+1}-1$
Acceleratory rate equations				
7	$P_{3/2}$	Mampel power law	$\frac{2}{3}\alpha^{\frac{-1}{2}}$	$\alpha^{\frac{3}{2}}$
8	$P_{1/2}$	Mampel power law	$2\alpha^{\frac{1}{2}}$	$\alpha^{\frac{1}{2}}$
9	$P_{1/3}$	Mampel power law	$3\alpha^{\frac{2}{3}}$	$\alpha^{\frac{1}{3}}$
10	$P_{1/4}$	Mampel power law	$4\alpha^{\frac{3}{4}}$	$\alpha^{\frac{1}{4}}$
11	E_1	Exponential law	α	$ln\alpha$
Sigmoidal rate equations				
12	A_1, F_1	Avrami–Erofeev equation	$(1-\alpha)$	$-ln\,(1-\alpha)$
13	$A_{3/2}$	Avrami–Erofeev equation	$\frac{3}{2}(1-\alpha)(-\ln(1-\alpha))^{\frac{1}{3}}$	$[-\ln\,(1-\alpha)]^{\frac{2}{3}}$
14	A_2	Avrami–Erofeev equation	$2(1-\alpha)(-\ln(1-\alpha))^{\frac{1}{2}}$	$[-\ln\,(1-\alpha)]^{\frac{1}{2}}$
15	A_3	Avrami–Erofeev equation	$3(1-\alpha)(-\ln(1-\alpha))^{\frac{2}{3}}$	$[-\ln\,(1-\alpha)]^{\frac{1}{3}}$
16	A_4	Avrami–Erofeev equation	$4(1-\alpha)(-\ln(1-\alpha))^{\frac{3}{4}}$	$[-\ln\,(1-\alpha)]^{\frac{1}{4}}$
17	A_u	Prout-Tomkins equation	$\alpha(1-\alpha)$	$ln\left[\frac{\alpha}{1-\alpha}\right]$
Phase boundary reaction				
18	R_1, F_0, P_1	Power law	$(1-\alpha)^0$	α
19	R_2, $F_{1/2}$	Power law	$2(1-\alpha)^{\frac{1}{2}}$	$1-(1-\alpha)^{\frac{1}{2}}$
20	R_3, $F_{2/3}$	Power law	$3(1-\alpha)^{\frac{2}{3}}$	$1-(1-\alpha)^{\frac{1}{3}}$
Diffusion mechanism				
21	D_1	Parabola law	$\frac{1}{2}\alpha$	α^2
22	D_2	Valensi equation	$[-\ln\,(1-\alpha)]^{-1}$	$\alpha+(1-\alpha)ln(1-\alpha)$
23	D_3	Jander equation	$\frac{3}{2}(1-\alpha)^{\frac{2}{3}}\left[1-(1-\alpha)^{\frac{1}{3}}\right]^{-1}$	$\left[1-(1-\alpha)^{\frac{1}{3}}\right]^2$

4. Results and discussion

4.1. Thermal behaviour of PVC and iron oxides-PVC mixtures

4.1.1. Thermal behaviour of pure PVC pyrolysis

The TGA and differential thermogravimetric (DTG) profiles of pure PVC degradation are presented in Figure 2 (A). PVC decomposes following three degradation stages. The first two overlapped stages having an onset temperature of 272 °C and a mass loss of 65% are mainly attributed to the de-hydrochlorination of PVC and the emission of gaseous HCl [23]. However, a portion of this loss is also associated with the evolution of H_2 [24], benzene, toluene, and other hydrocarbons [25]. This accounts for the increased mass loss above the theoretical content of HCl (58.3 wt%) in the PVC monomer. After the first two stages, the PVC chain is almost entirely stripped from its chlorine content [25]. The reaction describing the first two stages might thus be written as follows:

$$(\text{—}CH_2\text{—}CHCl\text{—}CH_2\text{—}CHCl\text{—})_n \rightarrow (\text{—}HC{=}CH\text{—}CH{=}CH\text{—})_n + 2HCl \quad (1)$$

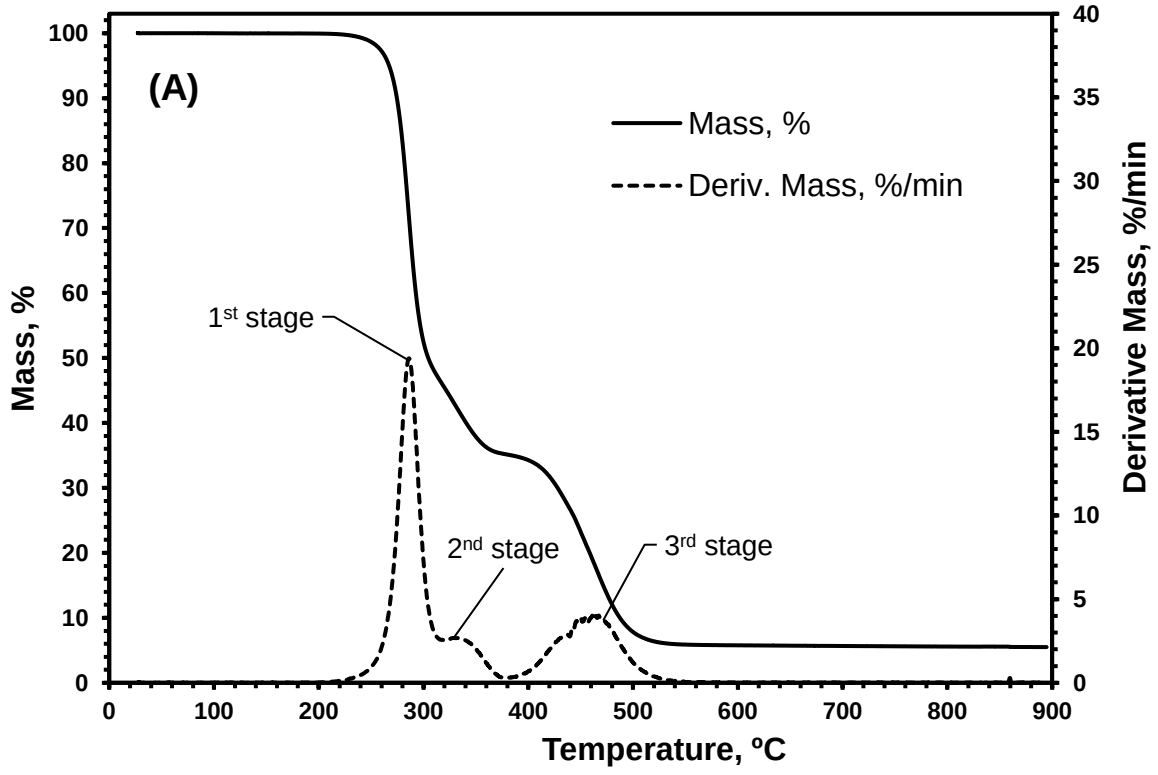

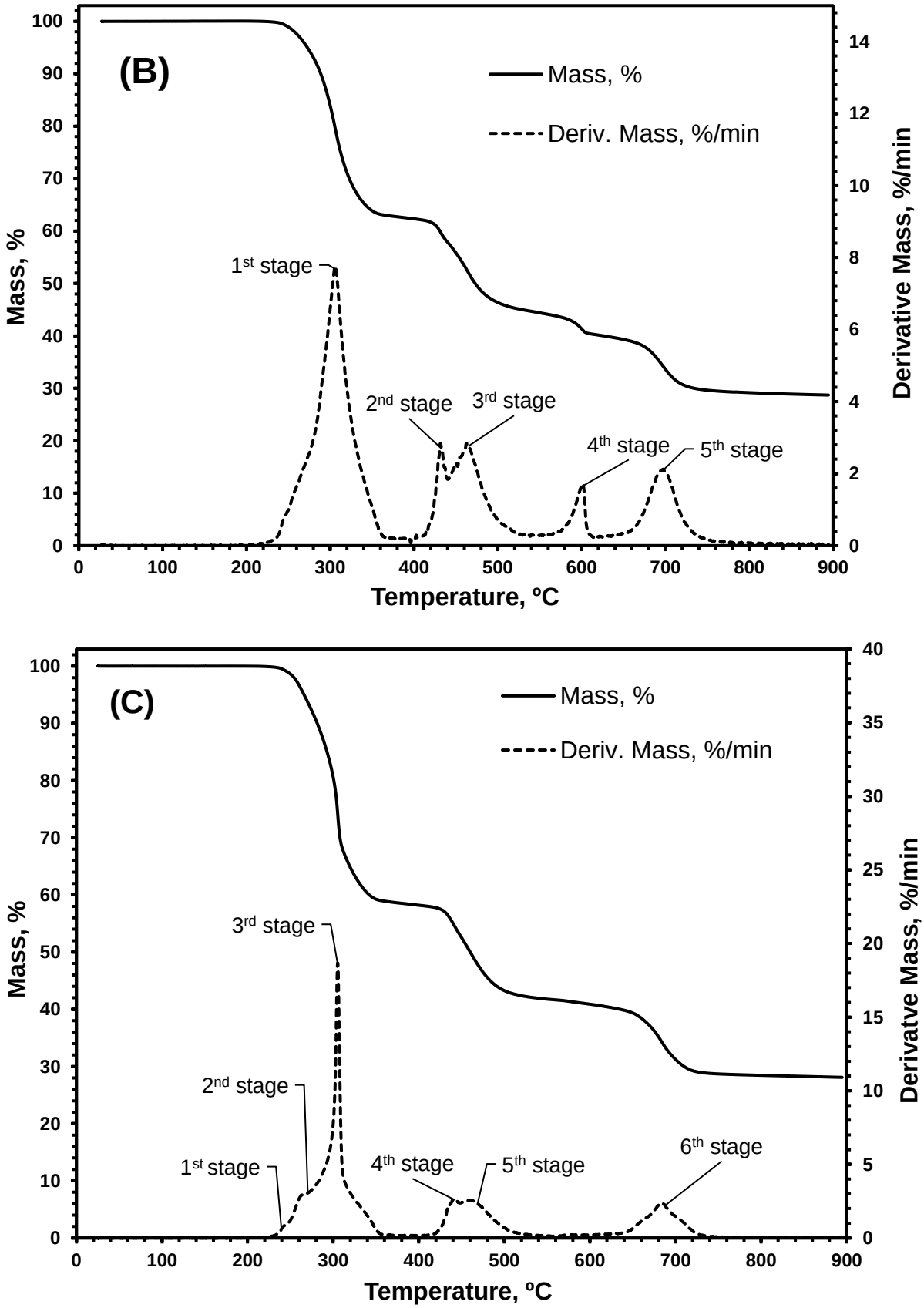

Figure 2: TGA/DTG profiles of pure PVC (A), Fe_3O_4-PVC (31.6 wt% Fe_3O_4) (B) and Fe_2O_3-PVC (29.9 wt% Fe_2O_3) (C) degradation under a nitrogen flow of 100 mL/min and at a heating rate of 10 K/min.

The solid residue left after the first two stages is polyene [23]. Formed polyene sequences then start degrading at 423 °C (third stage) into unsubstituted aromatics, alkyl aromatics and solid char [26]. H_2 has also been reported to evolve from this stage as well [24]. The third stage could be written according to the following chemical reaction [24]:

Polyene → H_2 + volatiles + char (2)

A residual mass of about 6% remains in the crucible after the thermal cracking of the PVC backbone, which as mentioned earlier, is characterised to be char [26]. Both the PVC de-hydrochlorination and the polyene thermal cracking stages show endothermic events with the former showing larger one (Figure 3, peaks 1 and 4).

Table 2: The mean particle size of the feed materials used in this work before any processing (e.g., mixing, tumbling etc.).

Material	Particle size, μm
PVC	158.8 ± 18.5
Fe_3O_4	31.7 ± 5.0
Fe_2O_3	36.6 ± 4.8

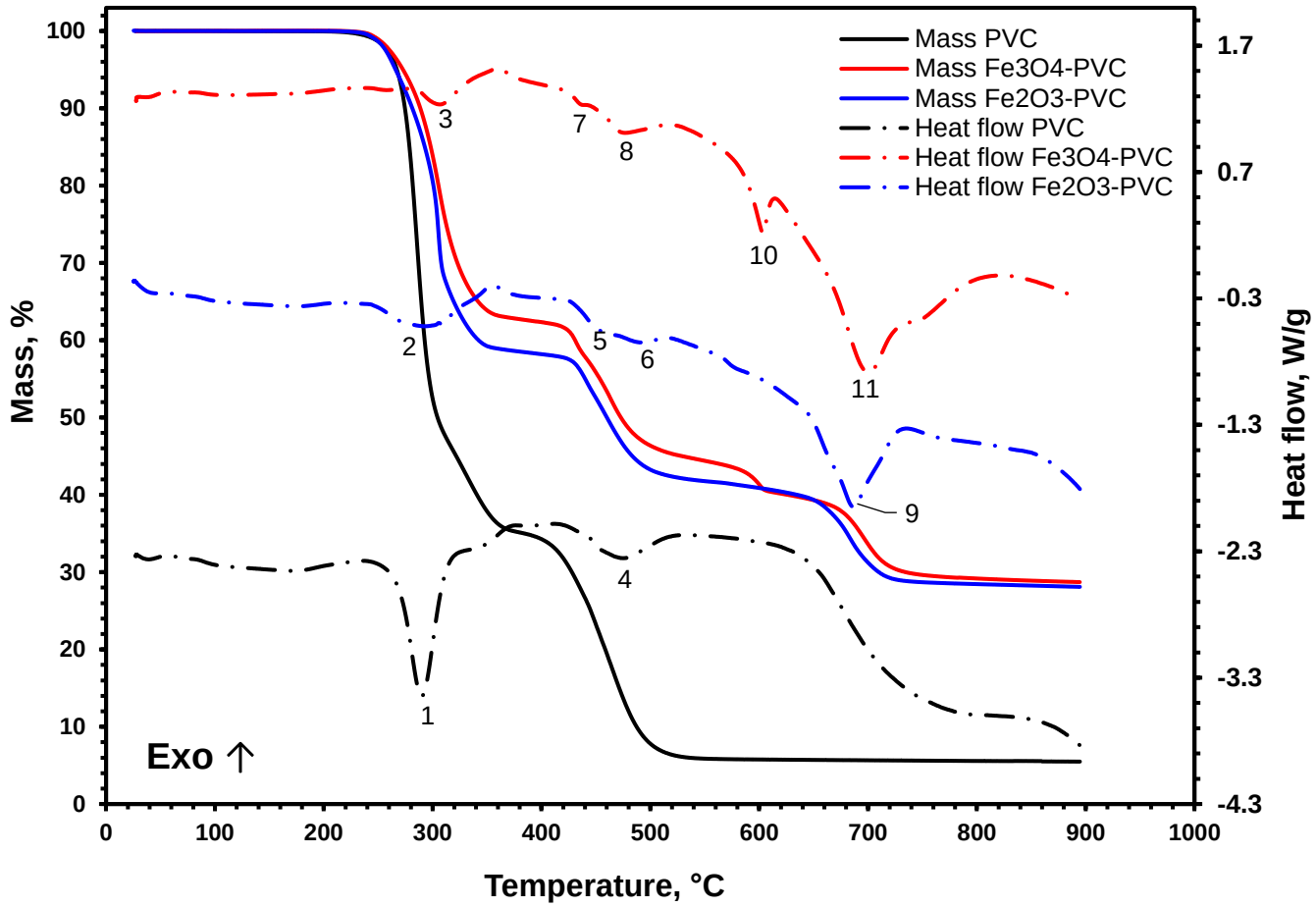

Figure 3: TGA/DSC profiles of pure PVC, Fe_3O_4-PVC (31.6 wt% Fe_3O_4), and Fe_2O_3-PVC (29.9 wt% Fe_2O_3) under a nitrogen flow of 100 mL/min and a heating rate of 10 K/min.

4.1.2. Thermal behaviour and reaction products of Fe_3O_4-PVC pyrolysis

The addition of a stoichiometric amount of Fe_3O_4 to PVC resulted in a significant change to the thermogravimetric profile of the PVC degradation. The decomposition of the Fe_3O_4-PVC mixture follows five degradation/reduction stages, instead of three as in the case of pure PVC (Figure 2 (B)).

The first stage starting at 274 °C is attributed to the de-hydrochlorination of PVC (HCl evolution) and the emission of H_2O from the chlorination of Fe_3O_4 (Reaction 3) [24]. It is evident from the profile presented in Figure 5 (D) that the chlorination of Fe_3O_4 by HCl is thermodynamically favourable where it shows negative Gibbs free energy values up to a temperature of 580 °C. The profiles presented in Figure 3 suggest that the addition of Fe_3O_4 to PVC did not significantly affect the onset de-hydrochlorination temperature. However, this

addition did hamper the decomposition speed thus creating higher stability than in the case of pure PVC. Further evidence of this hampering effect is presented in the kinetic section 4.2.1. The chlorination reaction can be written as follows:

$Fe_3O_4 + 2HCl \rightarrow FeCl_2 + Fe_2O_3 + H_2O$, $\Delta H = -108.0$ kJ/mol at T = 300 °C (3)

Despite the exothermic nature of this reaction, no exothermic peak was detected from the DSC measurement (Figure 3). This can be assigned to the highly endothermic nature of PVC de-hydrochlorination which could mask the exothermic chlorination event (Figure 3, peak 1). Nonetheless, the chlorination of Fe_3O_4 by HCl is confirmed from the XRD pattern presented in Figure 4 for the pyrolysis of the Fe_3O_4-PVC mixture at different pyrolysis temperatures. It is clear that the iron chloride species appears in the hydrate form (Rokuehnite; $FeCl_2.2H_2O$) with low intensity peaks, while no Lawrencite ($FeCl_2$) peaks can be seen at 400 °C (Pattern B). However, as the temperature of the pyrolysis increases to 550 and 650 °C, more prominent peaks of $FeCl_2.2H_2O$ are seen and the peaks associated with $FeCl_2$ start to appear showing very high intensity at 650 °C (Figure 4, Pattern D). The formation of $FeCl_2$ was also detected under the SEM for the 650 °C residue where $FeCl_2$ crystals appeared in the form of thin cylindrical discs (Figure S1 supplementary material). These discs could not be seen in the residue at a temperature of 400 °C which agrees with the absence of $FeCl_2$ peaks in the 400 °C XRD pattern in Figure 4. In the works performed by Kanungo [27] and Louvain et al. [28] the de-hydration behaviour of $FeCl_2.4H_2O$ was studied. Kanungo [27] reported that the de-hydration takes place in three steps where two water moles are lost in the first step followed by losing one mole in each of the following steps such that the material is completely de-hydrated at a temperature of 183 °C at a heating rate of 6 °C/min under flowing nitrogen. A similar behaviour was reported by Louvain et al. [28] whereby the mass loss associated with the de-hydration of $FeCl_2.4H_2O$ was completed at about 180 °C under nitrogen and at a heating rate of 5 °C/min. Louvain et al. [28] even managed to isolate $FeCl_2.2H_2O$ and exposed it to a thermogravimetric

scan. In that work [28], $FeCl_2.2H_2O$ showed a clear mass loss which peaked at 134 °C. Such a mass loss can potentially be assigned to the de-hydration. Hence, the peaks associated with $FeCl_2.2H_2O$ appearing at high temperatures in Figure 4 can potentially be regarded to the hydration of $FeCl_2$ present in the post pyrolysis residue; the increased amount of $FeCl_2.2H_2O$ with temperature can be attributed to the increased amount of formed $FeCl_2$ which is then hydrated.

Reaction 3 suggests that aside to the formed $FeCl_2$, hematite (Fe_2O_3) should also be seen in the 400 °C pattern (Figure 4, pattern B). The absence of Fe_2O_3 peaks in Figure 4 is attributed to the direct reduction of Fe_2O_3 into Fe_3O_4 by the emitted H_2 gas during the de-hydrochlorination stage according to Reaction 4. This reaction shows a negative Gibbs free energy over the entire temperature range suggesting that it is thermodynamically favourable. Moreover, the reduction of Fe_2O_3 by H_2 was previously reported to take place at a temperature as low as 218 °C, however, it showed slow kinetics up to 309 °C [29].

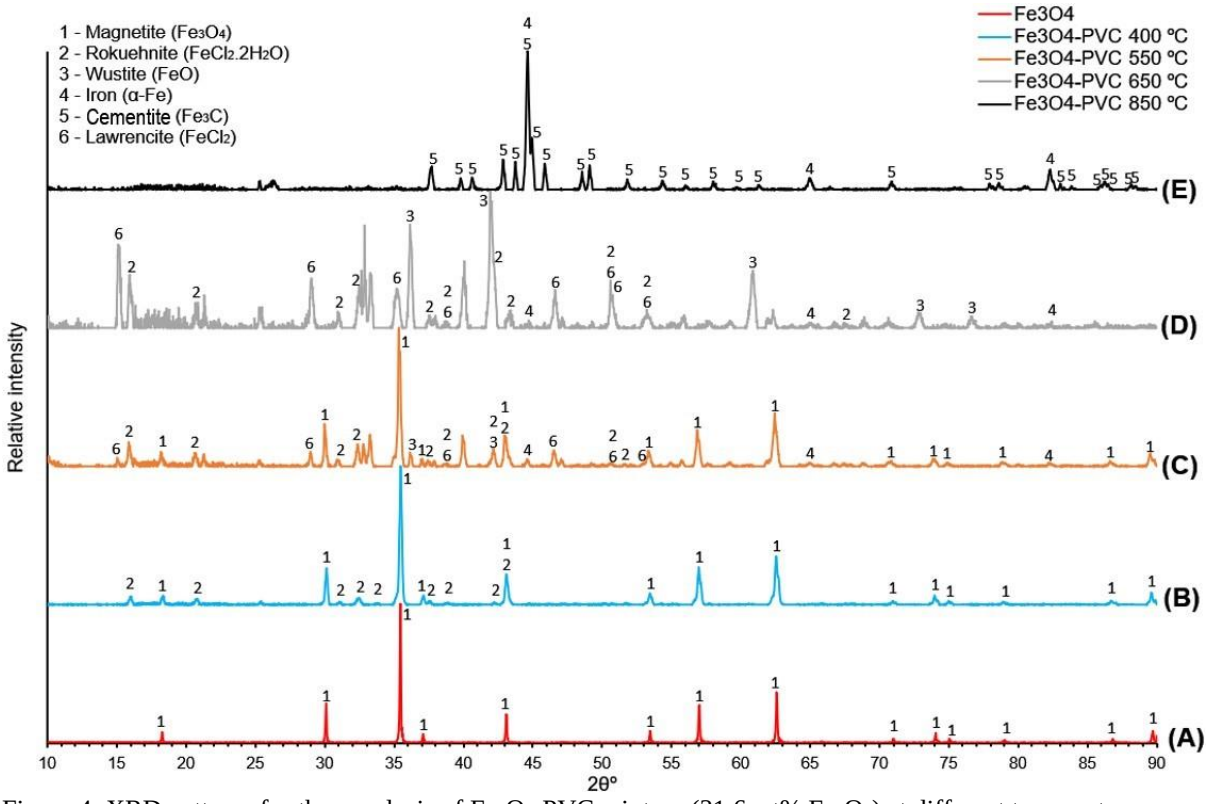

Figure 4: XRD patterns for the pyrolysis of Fe_3O_4-PVC mixture (31.6 wt% Fe_3O_4) at different temperatures.

In the second stage ranging from 410 to 440 °C (Figure 2 (B)), polyene sequences decompose to form char, volatiles, and H_2 [24]. In the presence of Fe_3O_4, $(CO)_x$ was reported to form as well [24]. In stage 3 (440 – 520 °C), formed char, H_2, and CO (from reduction) can then partially react with Fe_3O_4 to form small amounts of FeO which is then partially reduced into α-Fe according to reactions 15, 17, 20, and 22. The peaks of both FeO and α-Fe can be seen in Figure 4 (Pattern C) confirming these reactions. The thermodynamics of these reactions, while being endergonic ($0 < \Delta G$), they can still be driven forward since ΔG has small positive values of 14.5, 2.5, 23.8, and 45.1 kJ/mol at a temperature of 460 °C for reactions 15, 17, 20 and 22, respectively. The positive value of ΔG also explains why the peaks of FeO and α-Fe are very small as these reactions are majorly directed backwards. In literature, the in situ XRD analysis performed by Pineau et al. [30] also suggested the possibility of the co-existence of Fe_3O_4, FeO, and Fe for the reduction system of Fe_3O_4 under H_2 in the temperature window 390 – 570 °C. This temperature range overlaps with the range reported here. After that, the reduction of FeO to Fe by CO (reaction 24) is thermodynamically possible up to a temperature of 550 °C leading to the formation of α-Fe.

The overlapping between polyene cracking and the partial reduction of Fe_3O_4 is reflected in the thermal data as DTG and heat flow doublets (Figures 2 (B) and 3).

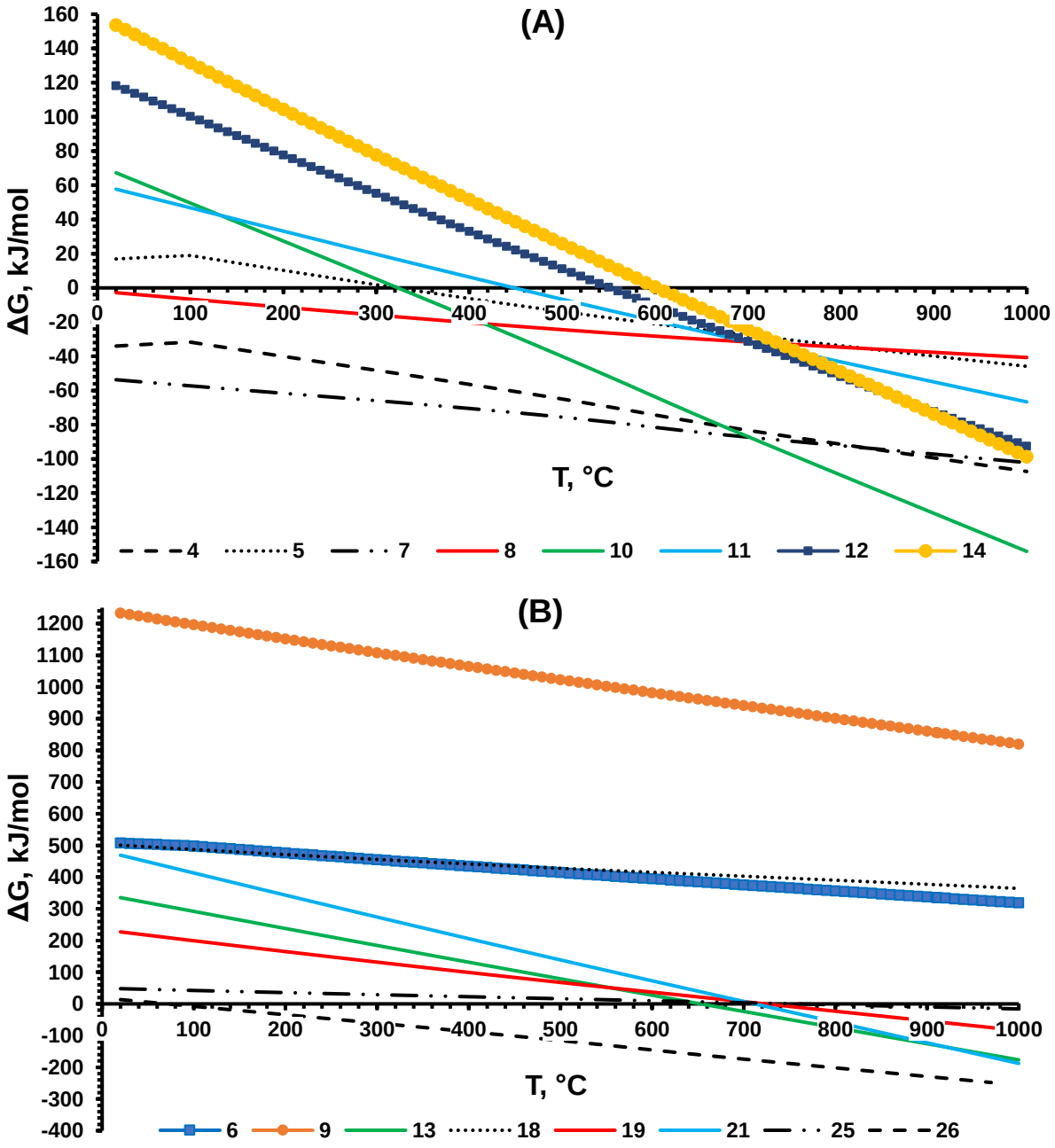
(A)
ΔG, kJ/mol
T, °C
4
5
7
8
10
11
12
14
(B)
ΔG, kJ/mol
T, °C
6
9
13
18
19
21
25
26

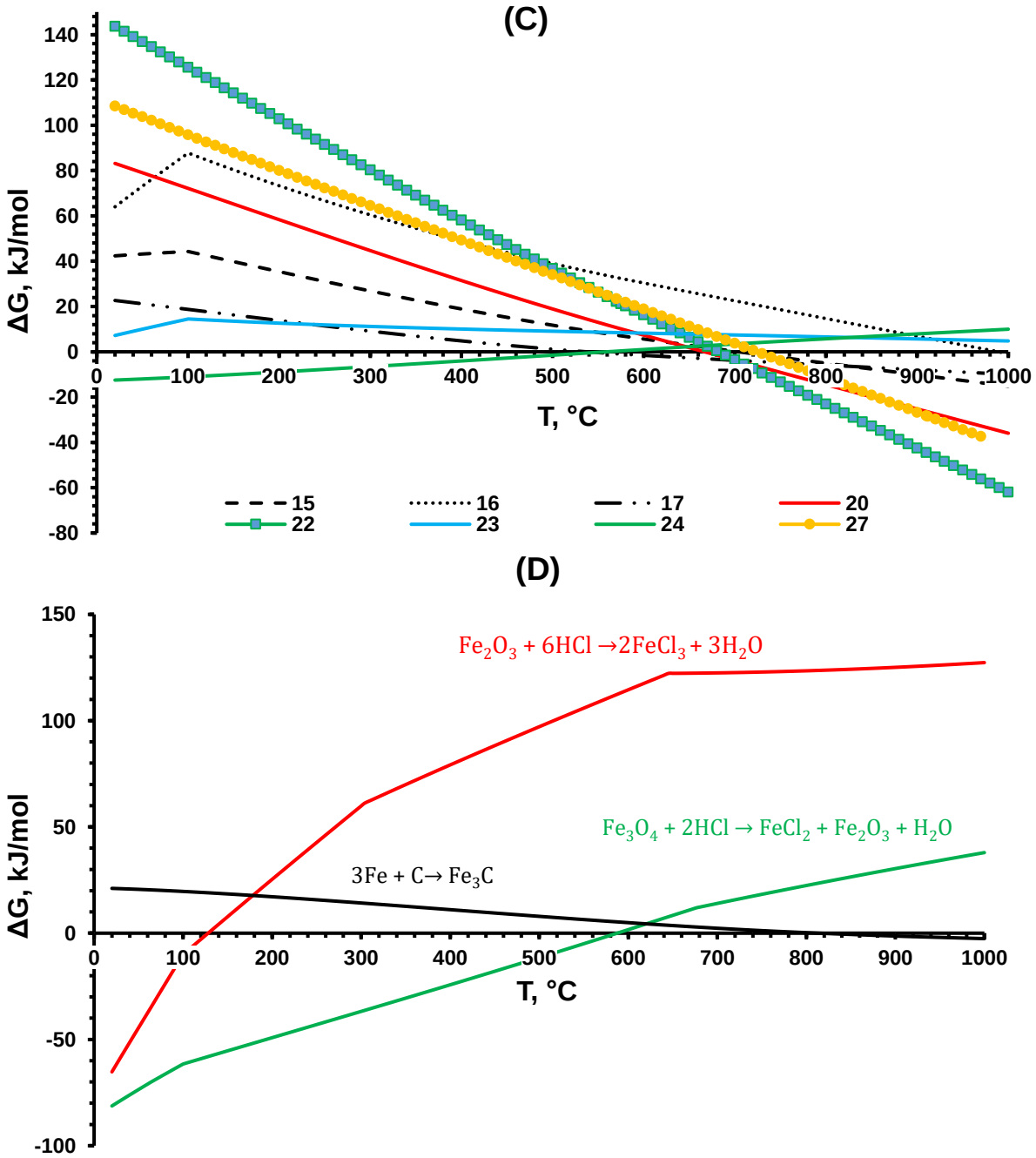

Figure 5: The change in the Gibbs free energy for the major chlorination and reduction reactions (4 – 28) occurring during the thermal degradation of PVC in the presence of Fe_3O_4 and Fe_2O_3.

$3Fe_2O_3 + H_2 \rightarrow 2Fe_3O_4 + H_2O$ (4)

$Fe_2O_3 + H_2 \rightarrow 2FeO + H_2O$ (5)

$Fe_2O_3 + H_2 \rightarrow 2Fe + H_2O + O_2$ (6)

$3Fe_2O_3 + CO \rightarrow 2Fe_3O_4 + CO_2$ (7)

$Fe_2O_3 + CO \rightarrow 2FeO + CO_2$ (8)

$2Fe_2O_3 + CO \rightarrow 4Fe + CO_2 + 2.5O_2$ (9)

$3Fe_2O_3 + C \rightarrow 2Fe_3O_4 + CO$ (10)

$Fe_2O_3 + 0.5C \rightarrow 2FeO + 0.5CO_2$ (11)

$Fe_2O_3 + C \rightarrow 2FeO + CO$ (12)

$Fe_2O_3 + 3C \rightarrow 2Fe + 3CO$ (13)

$Fe_2O_3 + 1.5C \rightarrow 2Fe + 1.5CO_2$ (14)

$Fe_3O_4 + H_2 \rightarrow 3FeO + H_2O$ (15)

$Fe_3O_4 + 4H_2 \rightarrow 3Fe + 4H_2O$ (16)

$Fe_3O_4 + CO \rightarrow 3FeO + CO_2$ (17)

$Fe_3O_4 + 2CO \rightarrow 3Fe + 2CO_2 + O_2$ (18)

$Fe_3O_4 + 2C \rightarrow 3Fe + 2CO_2$ (19)

$Fe_3O_4 + 1/2C \rightarrow 3FeO + 1/2CO_2$ (20)

$Fe_3O_4 + 4C \rightarrow 3Fe + 4CO$ (21)

$Fe_3O_4 + C \rightarrow 3FeO + CO$ (22)

$FeO + H_2 \rightarrow Fe + H_2O$ (23)

$FeO + CO \rightarrow Fe + CO_2$ (24)

$FeO + 0.5C \rightarrow Fe + 0.5CO_2$ (25)

$6Fe_2O_3 + C \rightarrow 4Fe_3O_4 + CO_2$ (26)

$FeO + C \rightarrow Fe + CO$ (27)

$3Fe + C \rightarrow Fe_3C$ (28)

In the temperature range 575 – 615 °C, a mass loss of about 4.0% can be seen (Figure 2 (B)). In that range, the reduction of Fe_3O_4 by char starts yielding FeO according to reactions 20 and 22. The change in the Gibbs free energy for these reactions is close to zero in that range at 7.4 and 16.3 kJ/mol for reactions 20 and 22, respectively suggesting that Fe_3O_4 and FeO can co-exist and hence FeO peaks intensity increase. However, released CO from reaction 22 can then react with Fe_3O_4 and transform it further into FeO at higher temperatures (650 °C) such as that seen in Figure 4 Pattern D with the thermodynamically favourable reaction 17 (Figure 5 (C)). The formation of FeO in large amounts is confirmed from the intense XRD peaks (Figure 4, pattern D). This reduction is also associated with the appearance of a sharp endothermic heat

flow in Figure 3 (peak 10). This endotherm is in line with the thermodynamics data since the enthalpy change for reactions 20 and 22 are +104.0 and +189.9 kJ/mol, respectively.

A further increase in temperature in the range 655 – 750 °C yields another mass loss of about 9.9% (Figure 2 (B)). At that point, formed FeO is reduced to α-Fe by char as shown in reactions 25 and 27. Both reactions 25 and 27 are almost at equilibrium (ΔG = 3.6 and 3.7 kJ/mol) at a temperature of 700 °C which suggests that α-Fe should start appearing alongside FeO. The results in the XRD, however, were collected at 850 °C, a temperature at which the presence of α-Fe is more favoured which explains the large α-Fe peaks. This mass loss is accompanied with a very large endothermic peak (Figure 3 peak 11) which is in agreement with the enthalpy change of reactions 25 and 27 at +65.8 and +151.3 kJ/mol, respectively at a temperature of 700 °C. A similar mass loss was reported by Ye et al. [24] for a Fe_3O_4-PVC mixture in which both CO and CO_2 gases where detected by a mass spectrometer in that temperature range. This is in line with reactions 25 and 27 containing CO and CO_2 as products. The formation of α-Fe is shown in Figure 4 Pattern E and is also confirmed in the SEM/EDS maps and spot analysis presented in Figure S2.

A portion of the formed α-Fe then reacts with the residual char to form cementite (Fe_3C) according to reaction 28 which is thermodynamically favourable above 820 °C. Fe_3C peaks are clearly shown in the XRD pattern (Figure 4 Pattern E).

4.1.3. Thermal behaviour and reaction products of Fe_2O_3-PVC pyrolysis

The TGA/DTG profiles of the Fe_2O_3-PVC mixture (29.9 wt% Fe_2O_3) are presented in Figure 2 (C). The degradation follows six stages instead of three and five as in the cases of pure PVC and Fe_3O_4-PVC, respectively. The initial large mass loss (first three stages) which is attributed to the de-hydrochlorination of PVC starts at about 275 °C with a mass loss of 41.0%. This mass loss is also associated with the evolution of H_2O along with HCl. In the work done by Zhang

et al. [31] it was reported that H_2O fragments start to appear in a mass spectrometer connected to a Fe_2O_3-PVC mixture at a temperature of about 277 °C. This H_2O emission can be related to the reduction of Fe_2O_3 by H_2 (Reaction 4) into Fe_3O_4 and the subsequent chlorination of formed Fe_3O_4 by HCl into $FeCl_2$ (Reaction 3). The occurrence of these reactions is confirmed from the XRD patterns presented in Figure 6 (Pattern B) where peaks of both $FeCl_2.2H_2O$ and Fe_3O_4 can be seen.

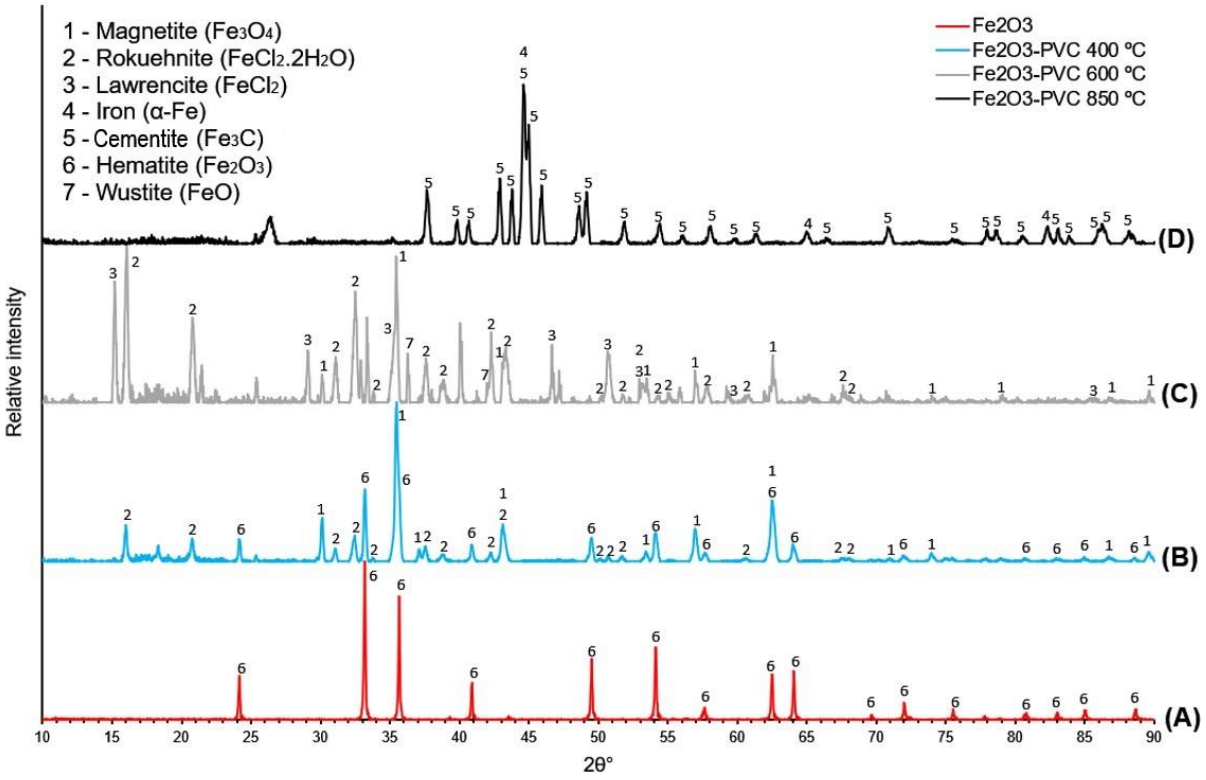

Figure 6: XRD patterns for the pyrolysis of Fe_2O_3-PVC mixture (29.9 wt% Fe_2O_3) at different temperatures.

When the temperature increases up to 600 °C, peaks of $FeCl_2$ start to appear and this temperature increase also results in a significant increase in the intensity of $FeCl_2.2H_2O$ XRD peaks. Likewise, it is believed that more $FeCl_2$ is formed at higher temperatures (which could be attributed to enhanced chlorination kinetics) after which it is hydrated into $FeCl_2.2H_2O$ when cooled down. The increase in the XRD peak intensity of $FeCl_2.2H_2O$ can also be confirmed from the SEM scans of the pyrolysis residue of Fe_2O_3-PVC at 600 °C which shows the growth of a large Monoclinic crystal of $FeCl_2.2H_2O$ (Figure 7). Spot analysis of this crystal is presented in Figure S3. The spot analysis shows atomic percentages of 37.6, 37.8, and 24.6% for iron,

oxygen, and chlorine, respectively suggesting their co-existence in one crystal. The deviation from the theoretical percentages present in the $FeCl_2.2H_2O$ molecule is due to contamination of the crystal by other minerals which is clearly shown in the secondary electron image of this crystal (Figure S4). The presence of crystals of this size in the 600 °C residue and their absence in the 400 °C residue explains the huge increase in the intensity of $FeCl_2.2H_2O$ in the XRD patterns (Figure 6).

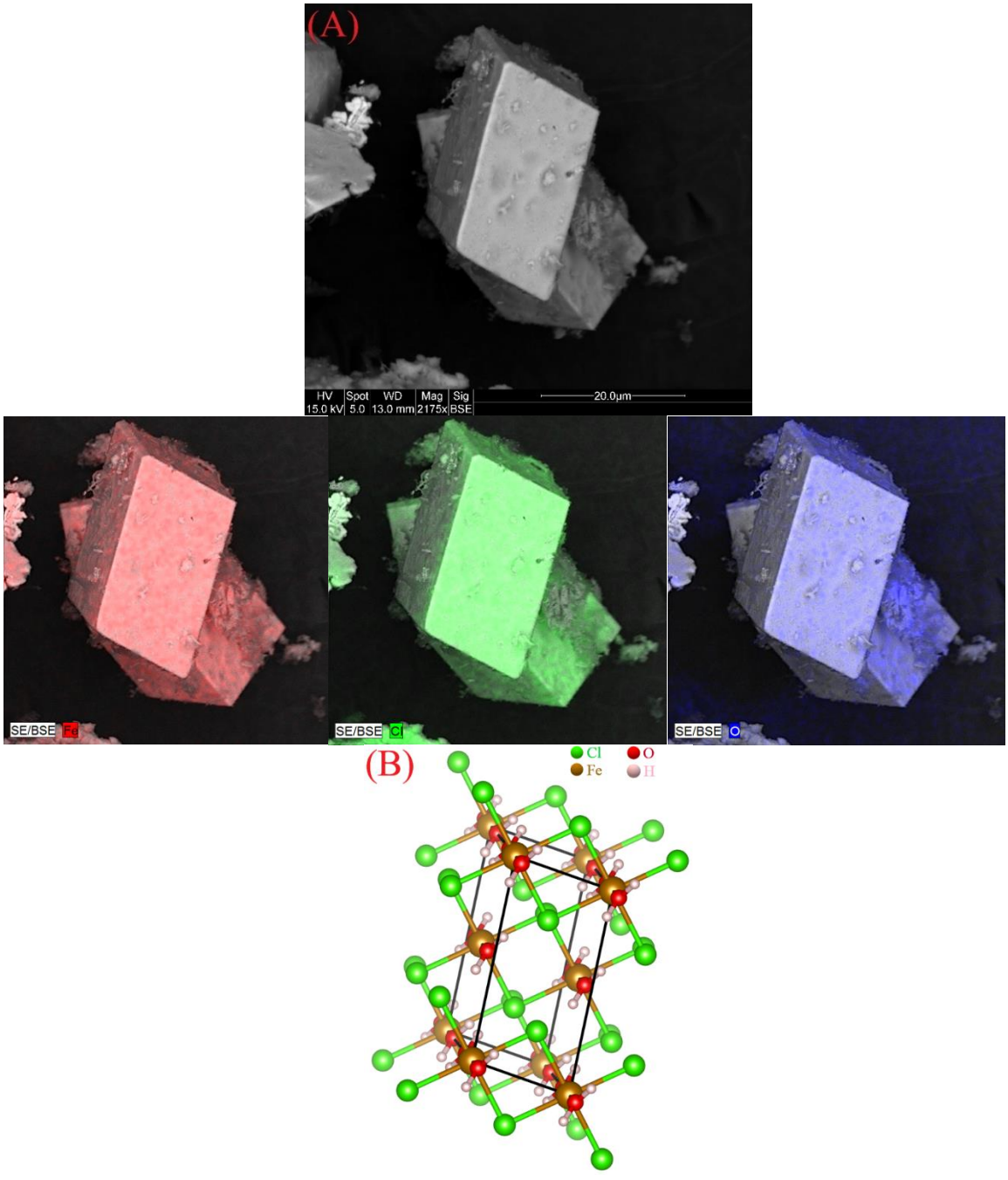

Figure 7: (A) Back scattered image of a large Monoclinic crystal of Rokuehnite ($FeCl_2.2H_2O$) along with EDS mapping formed in the post pyrolysis residue of Fe_2O_3-PVC mixture at 600 °C and (B) Monoclinic crystal lattice of Rokuehnite ($FeCl_2.2H_2O$) obtained from Crystallography Open Database (COD) and graphed using VESTA software [32, 33].

The de-hydrochlorination of PVC in presence of Fe_2O_3 showed an endothermic peak (Figure 3, peak 2). The intensity of this peak is much lower than that seen for pure PVC. This could be assigned to the exothermic nature of the reduction of Fe_2O_3 by H_2 occurring in the same temperature range resulting in a flatter endotherm.

The fourth and fifth overlapped stages extending from 415 to 512 °C (Figure 2 (C)) are associated with the simultaneous polyene thermal cracking and the reduction of Fe_2O_3 into Fe_3O_4 and FeO. The reduction into Fe_3O_4 occurs according to reactions 4, 7, 10, and 26 all of which have a negative ΔG in this temperature range. In these reactions, H_2, $C_{(s)}$, and CO react with Fe_2O_3 to form Fe_3O_4. The formation of FeO, in contrast, is majorly attributed to the reduction of Fe_2O_3 by gaseous H_2 and CO as shown in reactions 5 and 8 which are spontaneous in this temperature range. The reduction by $C_{(s)}$ can also contribute mildly to the formation of FeO in that range as well (reaction 11). All of these reactions are endothermic in this temperature range except reaction 7. The heat flow from these reactions can be seen in the endothermic doublet (peaks 5 and 6) appearing in Figure 3 such that the former peak is associated with polyene thermal cracking while the latter is associated with the reduction reactions.

After stages four and five, the residue does not contain Fe_2O_3 anymore, and FeO peaks started to appear (Figure 6, Pattern C). The final stage (sixth stage) extending in the temperature span 630 – 740 °C and showing a mass loss of 11.6% is associated with the carbothermic reduction of Fe_3O_4 and FeO. Fe_3O_4 is reduced to FeO according to reactions 20 and 22 which show values of ΔG that are very close to zero after which they shift to negative values with increase in temperature. A portion of Fe_3O_4 might also be reduced directly into Fe following reactions 19 and 21 (showing small positive ΔG values). The reduction of FeO by $C_{(s)}$ shown in reactions

25 and 27 have very small positive ΔG suggesting that FeO can transform into Fe. CO emitted from the reactions above can also reduce Fe_3O_4 to FeO and FeO to Fe as shown in reactions 17 and 24 where the former exhibit negative ΔG values in that range while the latter has very small positive (close to zero) ΔG.

This stage is accompanied by a large endothermic peak (peak 9, Figure 3) and the formation of α-Fe is clearly seen in Figure 6 (Pattern D). Having an endothermic heat flow in Figure 3 is in line with the thermodynamics data in which all these reactions exhibit a positive ΔH except for reaction 24. The reactions suggested here that are associated with the sixth stage are in a very good agreement with the results reported by Zhang et al. [31]. In that work, large peaks of CO and CO_2 appeared on a mass spectrometer in the same temperature range for a mixture of Fe_2O_3-PVC [31]. Finally, formed α-Fe reacts with excess char to form Fe_3C (Figure 6 Pattern D) according to reaction 28.

4.2. Non-isothermal pyrolysis kinetics

4.2.1. De-hydrochlorination kinetics of pure PVC, Fe_3O_4-PVC, and Fe_2O_3-PVC

In this section, stages one and two for pure PVC, stage one for Fe_3O_4-PVC and the first three stages for Fe_2O_3-PVC will be referred to as the "de-hydrochlorination stage". The usage of three different heating rates allows the calculation of the apparent activation energy using the model free approach. The de-hydrochlorination stages for PVC, Fe_3O_4-PVC, and Fe_2O_3-PVC at different heating rates are presented in Figures 8 (A), (B), and (C), respectively.

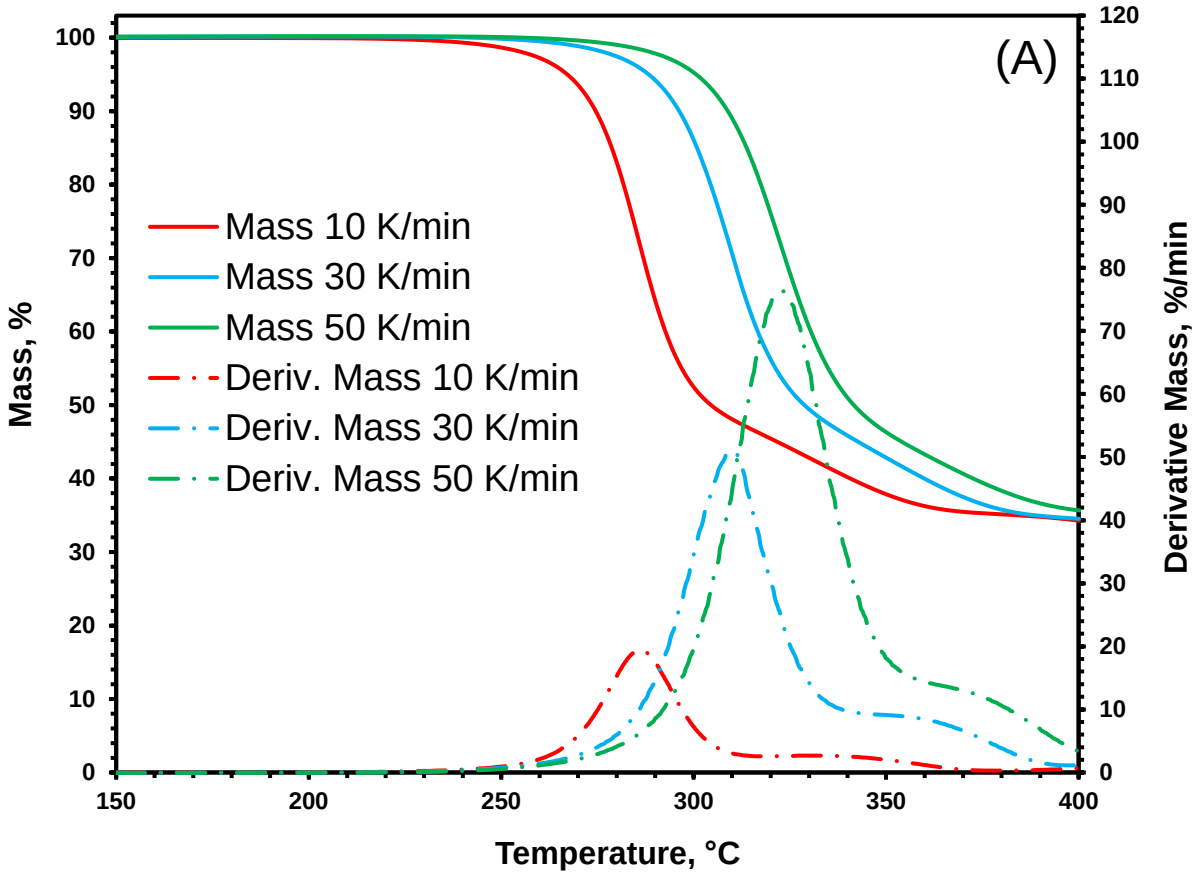
(A)
Mass 10 K/min
Mass 30 K/min
Mass 50 K/min
Deriv. Mass 10 K/min
Deriv. Mass 30 K/min
Deriv. Mass 50 K/min
Mass, %
Derivative Mass, %/min
Temperature, °C
100
90
80
70
60
50
40
30
20
10
0
120
110
100
90
80
70
60
50
40
30
20
10
0
150
200
250
300
350
400

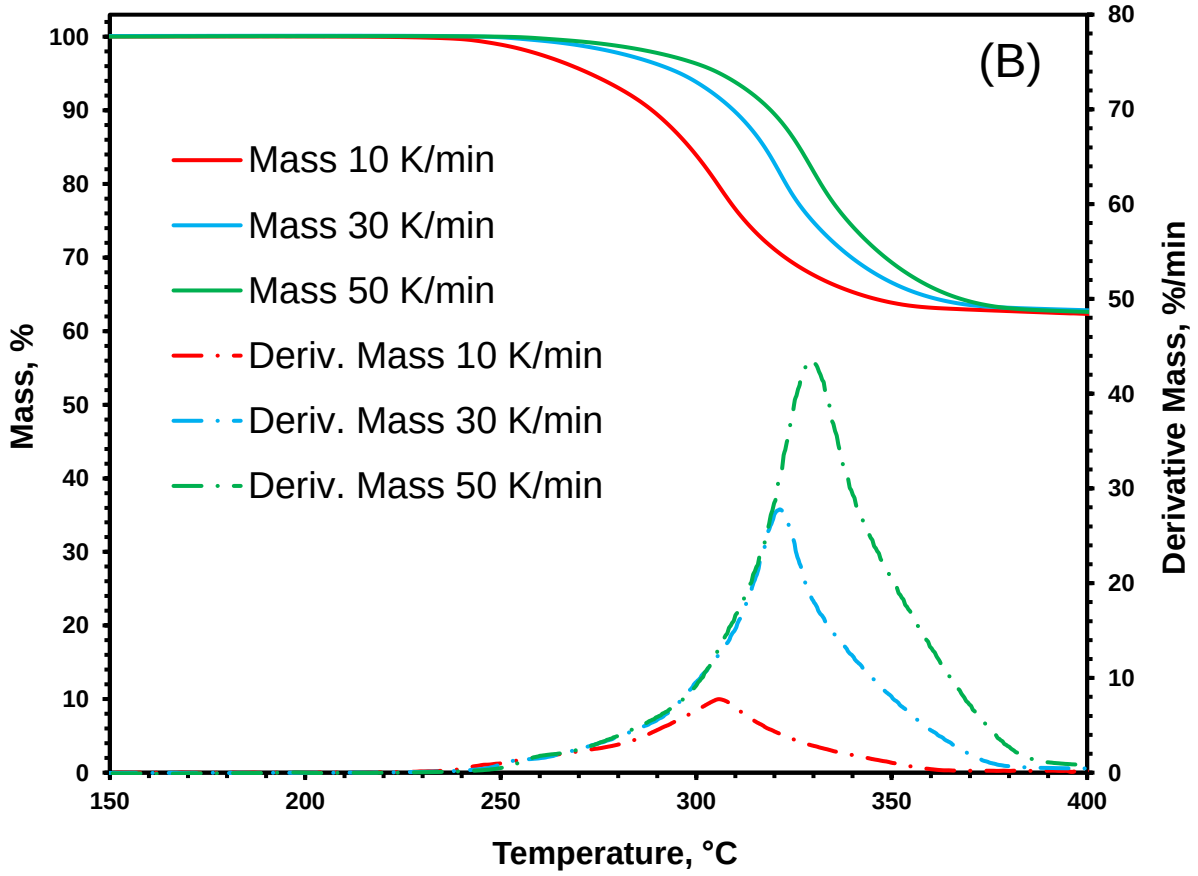
(B)
Mass 10 K/min
Mass 30 K/min
Mass 50 K/min
Deriv. Mass 10 K/min
Deriv. Mass 30 K/min
Deriv. Mass 50 K/min
Mass, %
Derivative Mass, %/min
Temperature, °C
100
90
80
70
60
50
40
30
20
10
0
80
70
60
50
40
30
20
10
0
150
200
250
300
350
400

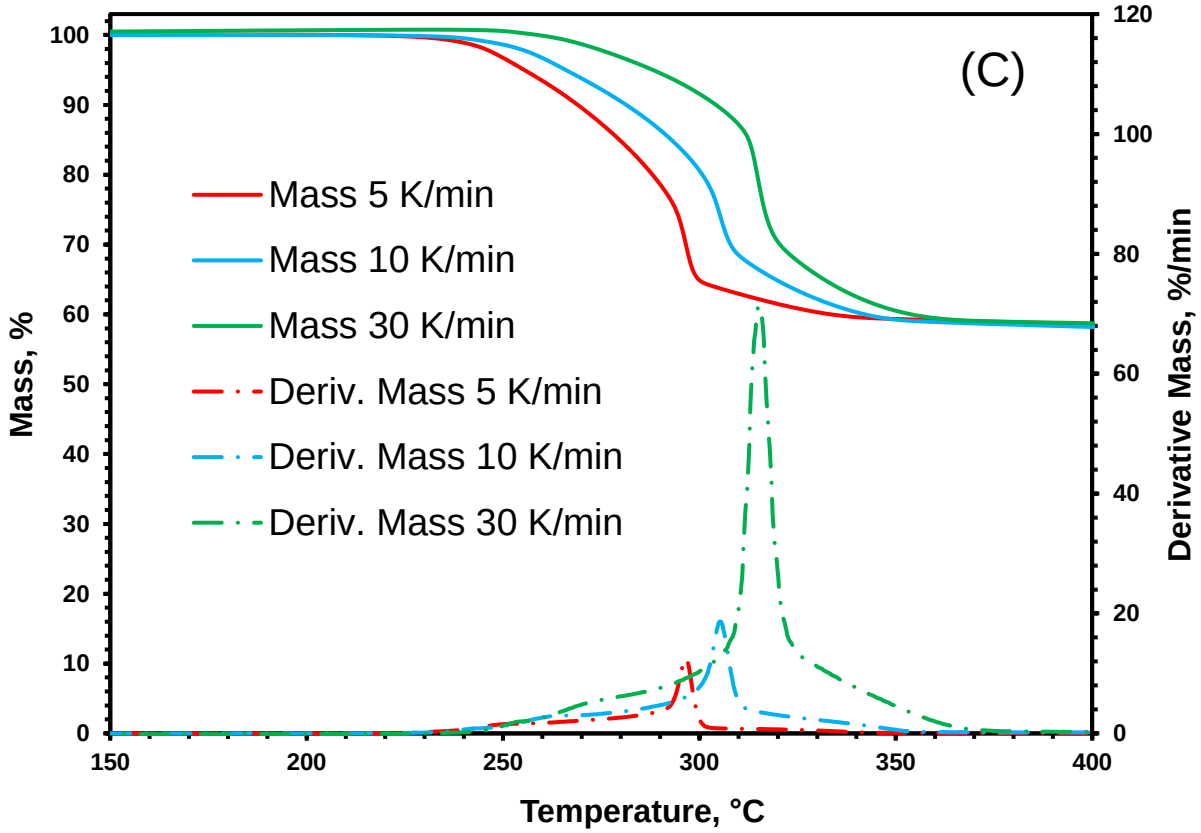

Figure 8: The de-hydrochlorination of pure PVC (A), Fe_3O_4-PVC (31.6 wt% Fe_3O_4) (B), and Fe_2O_3-PVC (29.9 wt% Fe_2O_3) (C) under a nitrogen flow of 100 mL/min and at different heating rates.

All the decomposition profiles in Figure 8 (A), (B), and (C) show a systematic lateral shift to a higher temperature at a fixed conversion level with an increase in the heating rate. Such a behaviour allows the utilisation of the iso-conversional principle mentioned earlier (section 3.2) for the determination of the apparent activation energy. Data obtained from these curves were fitted in the conversion range 0.1 – 0.9. Kinetic data fitting for PVC and its mixtures with Fe_3O_4 and Fe_2O_3 are presented in the supplementary material (Section 2).

The kinetic parameters associated with the de-hydrochlorination of pure PVC under an inert environment (N_2) are presented in Figures 9 (A) and (B).

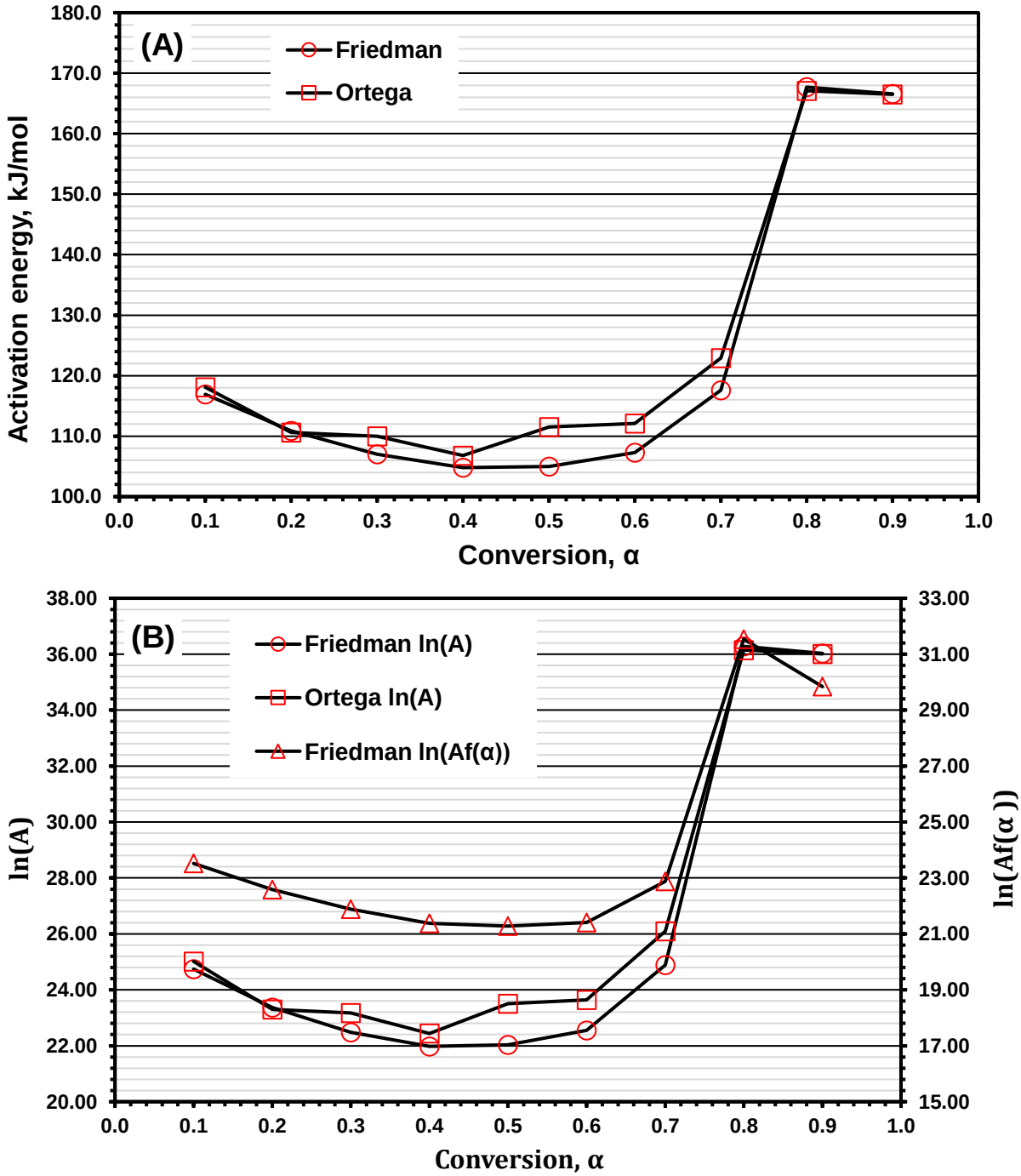

Figure 9: The apparent activation energy (A) and frequency factor (B) (unit of A and Af(α) is min^{-1}) associated with the de-hydrochlorination of PVC (first two stages in Figure 2 (A)).

Clearly from Figures 9 (A) and (B), a great agreement of the apparent activation energy and frequency factor calculated from Friedman (differential) and Ortega (integral) methods can be seen. The activation energies associated with the de-hydrochlorination of pure PVC in the conversion range 0.1 – 0.9, averaged at 122.6 ± 24.2 and 125.1 ± 22.8 kJ/mol calculated from Friedman and Ortega models, respectively. An insignificant variation in the value of the

activation energy in the conversion range 0.1 – 0.7 is observed suggesting a single controlling mechanism in that range.

Figure 10 shows some of the conversion functions (lines) along with data points generated for $f(\alpha)$ using the model free kinetic parameters (Equation 13; dots) at different conversions. For pure PVC, the $f(\alpha)$ obtained from the model free parameters (squares) overlaps with the reaction model "C" given as $f(\alpha) = 3.7\alpha(1-\alpha)^2$ in the conversion range 0.1 – 0.6 (Figure 10).

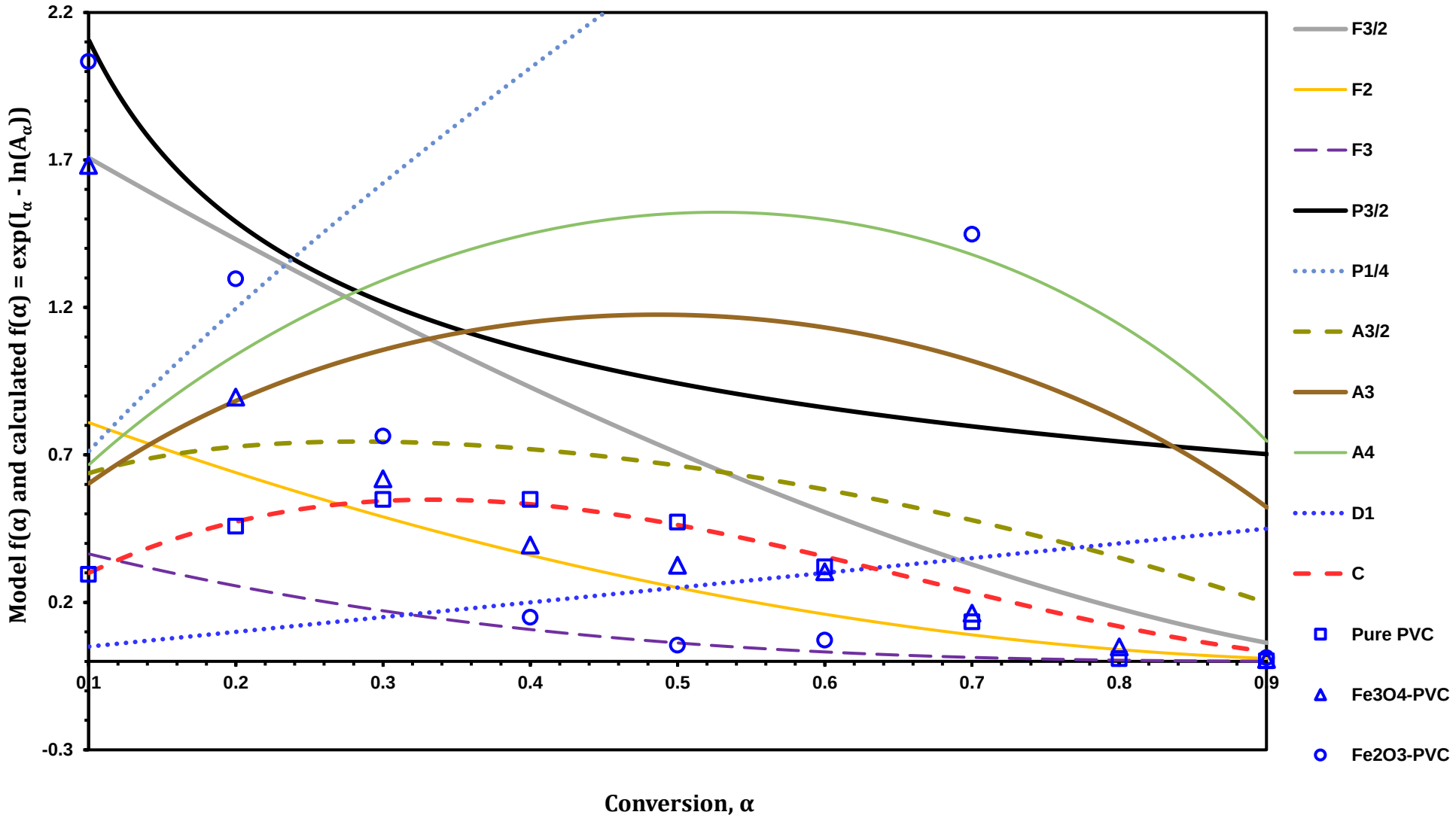

Figure 10: A plot of the reactions models presented in Table 1 against conversion and the corresponding f(α) values generated for the de-hydrochlorination stage of pure PVC, Fe_3O_4-PVC and Fe_2O_3-PVC using iso-conversional data (mechanism "C" is $f(\alpha) = 3.7\alpha(1-\alpha)^2$).

At a conversion of 0.7, experimental $f(\alpha)$ becomes very close to F_2 model and then overlaps with F_3 at α = 0.8 and 0.9. Previously [34], linear data fitting approach was used and the best fit obtained for PVC de-hydrochlorination was achieved using $f(\alpha) = \alpha(1-\alpha)^{2.13}$ in the conversion range 0.1 – 0.6 (A model very similar to the one obtained here from the model free kinetic data). The reaction model reported in this work (Figure 10) follows the truncated form of the Šesták and Berggren [17, 18] which is also known as the extended Prout-Tomkins model ($f(\alpha) = \alpha^m(1-\alpha)^n$) [18]. The truncated Šesták and Berggren model is considered an example of an auto-catalytic model [18]. This agrees with the fact that the de-hydrochlorination of PVC was characterised as an auto-catalytic process where released HCl was found to contribute to accelerating the de-hydrochlorination process [35]. This effect eventually disappears which is evident from the increase in the activation energy at 0.7 < α along with the change in the reaction model towards mechanisms F_2 and F_3.

The addition of a stoichiometric amount of Fe_3O_4 to PVC (31.6 wt% Fe_3O_4) resulted in a significant increase in the apparent activation energy for the de-hydrochlorination Figures 11 (A) and (B).

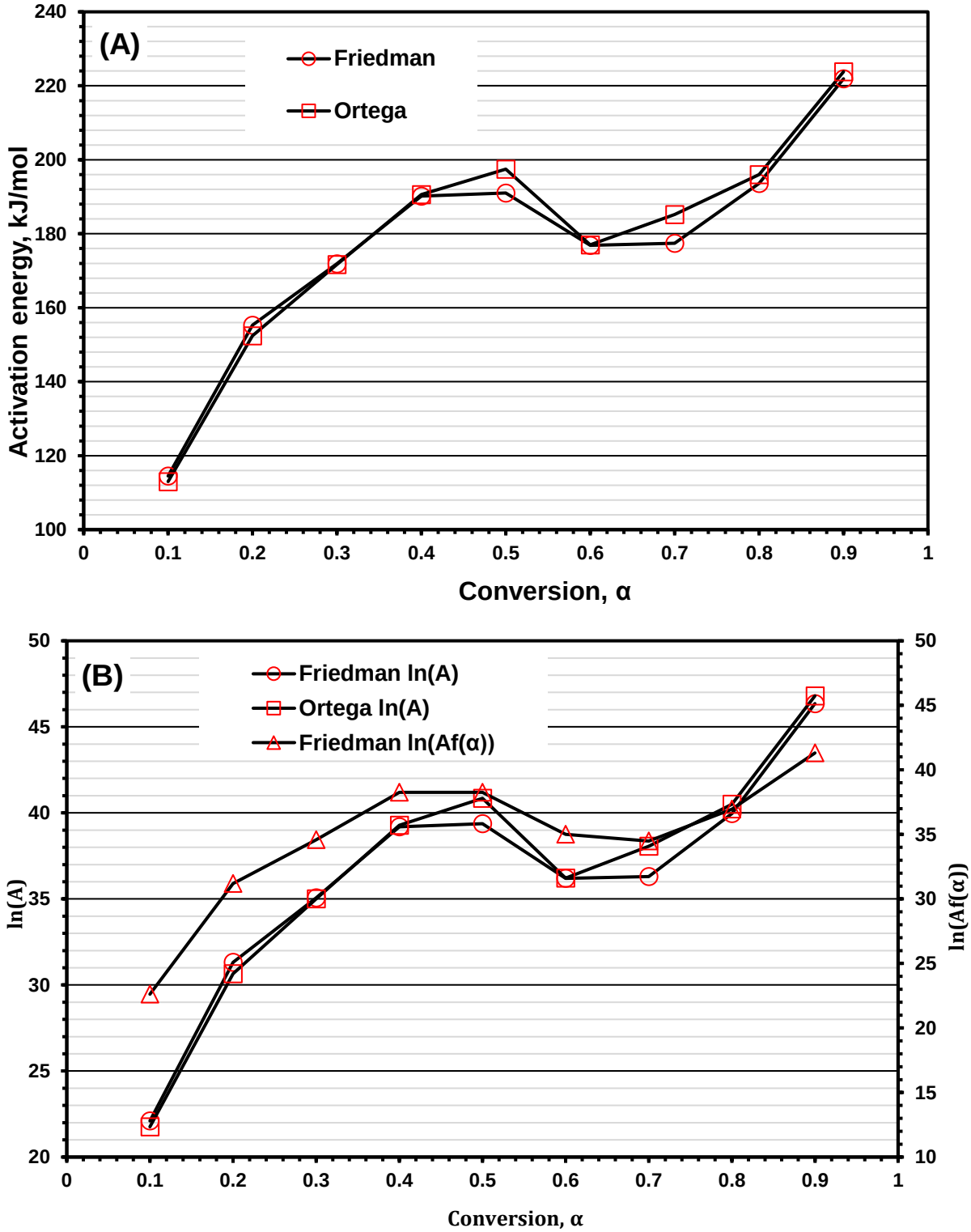

Figure 11: The apparent activation energy (A) and frequency factor (B) (unit of A and Af(α) is min^{-1}) associated with the de-hydrochlorination of Fe_3O_4-PVC (first stage in Figure 2 (B)).

At a conversion of 0.1, the apparent activation energy starts at a value that is very similar to that seen for pure PVC at 114.5 and 113.0 kJ/mol calculated from Friedman and Ortega, respectively. However, at lower conversion values associated with the initiation of the de-

hydrochlorination (α = 0.004), the activation energy for Fe_3O_4-PVC mixture is much higher than that of pure PVC at 204.2 kJ/mol (Fe_3O_4-PVC) compared to 109.9 kJ/mol (pure PVC) at the same conversion. This suggests that a significant change in the initiation mechanism of the de-hydrochlorination has taken place when Fe_3O_4 was added to PVC. As the reaction progresses above a conversion of 0.1, a significant increase appears in the activation energy with it subsequently reaching a value of 191.0 kJ/mol at a conversion of 0.5 compared to 105.0 kJ/mol for pure PVC (Friedman) at the same conversion. Judging from the XRD and SEM data presented in earlier sections, the change in the apparent activation energy can be assigned to the capturing of released HCl by Fe_3O_4 to form $FeCl_2$ which can prohibit the auto-catalytic effect of HCl on the degradation of PVC. In this case, Fe_3O_4 works as a HCl scavenger which can fully or at least partially prevent the emitted HCl from forming polyenyl cation radicals which have been shown to be necessary for increasing the decomposition rate (Figure 12 (A)) [35]. Such an effect can translate in the form of an increase in the activation energy. A mechanism illustrating the inhibiting effect of Fe_3O_4 by capturing emitted gaseous HCl is presented in Figure 12 (B).

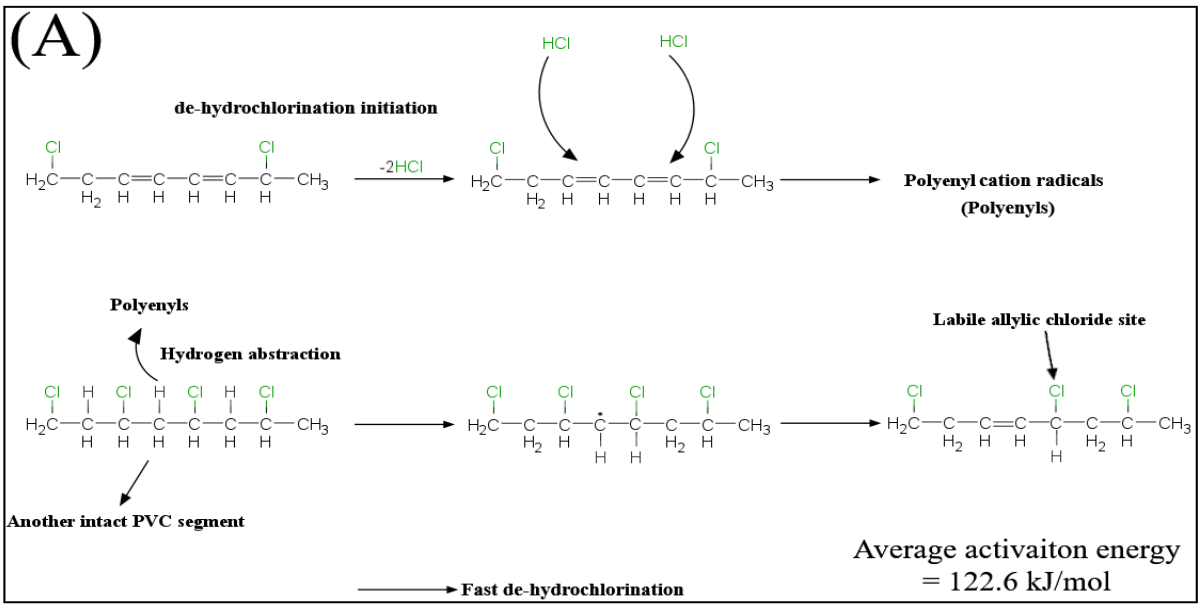

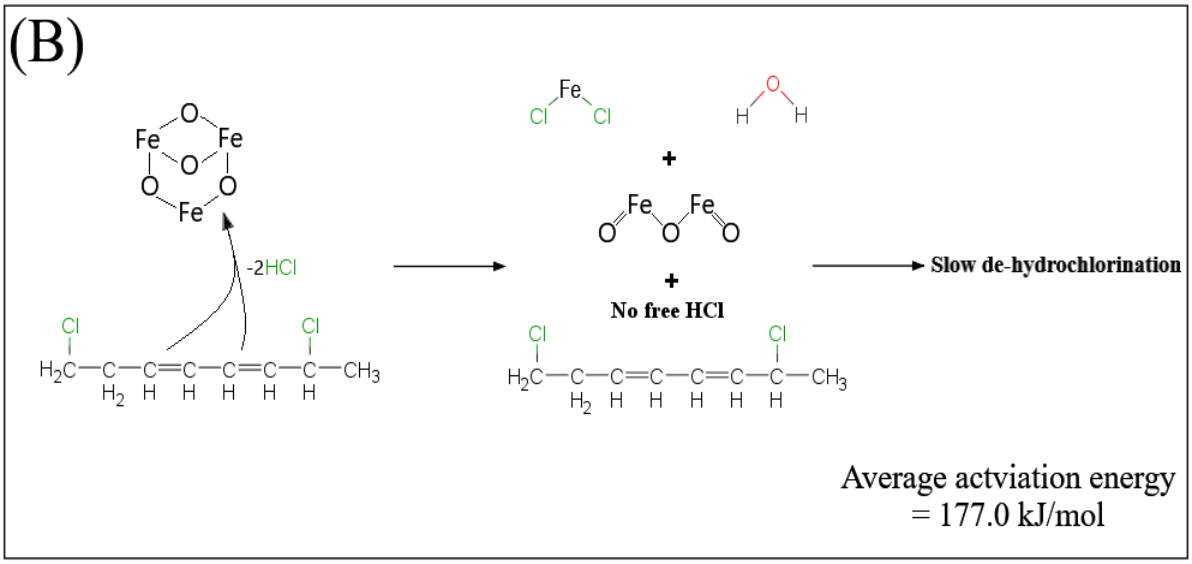

Figure 12: (A) Auto-catalysis mechanism of PVC de-hydrochlorination suggested by Starnes and Ge [35] and (B) The role of Fe_3O_4 in inhibiting the catalytic activity of HCl.

The complexity of the degradation of Fe_3O_4-PVC mixture can be seen from the continuous shift of the reaction model from one mechanism to another (Figure 10; triangles). Such behaviour can be assigned to the occurrence of many concurrent/sequential mass losses during the de-hydrochlorination such that $f(\alpha)$ overlaps with more than one mechanism below $\alpha = 0.4$ then settles at values close to F_2 model between $0.4 < \alpha < 0.9$ except for $\alpha = 0.6$ where it overlaps with D_1.

Fe_2O_3 showed a larger impact on the apparent activation energy of PVC de-hydrochlorination compared to Fe_3O_4. Likewise, the initiation activation energy increased from 109.9 to 215.1 kJ/mol when Fe_2O_3 was added ($\alpha = 0.004$). The variation of the apparent activation energy and frequency factor for Fe_2O_3-PVC de-hydrochlorination are shown in Figures 13 (A) and (B). Due to very poor data fitting at $\alpha = 0.8$, the kinetic parameters at that conversion were not included.

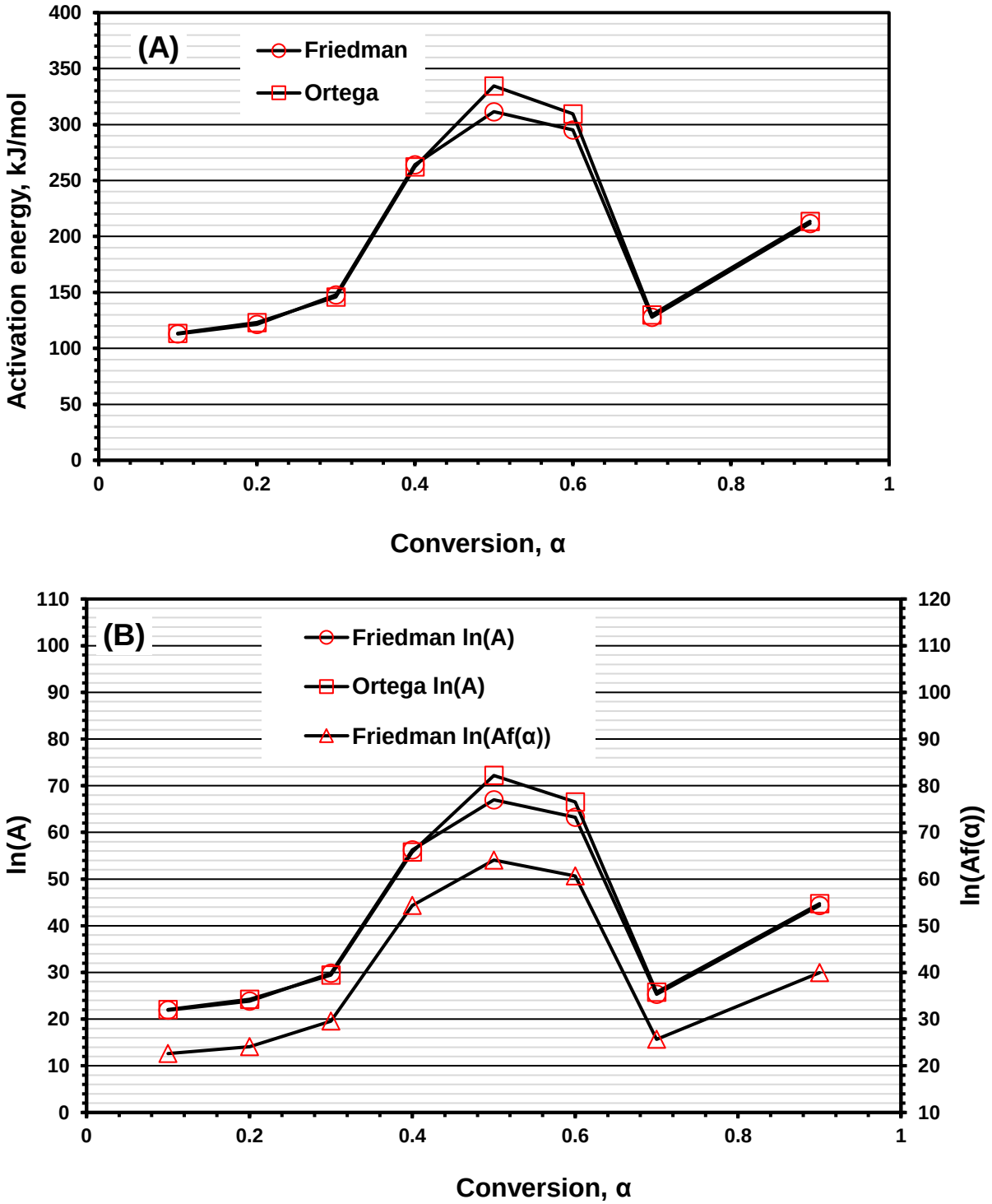

Figure 13: The apparent activation energy (A) and frequency factor (B) (unit of A and Af(α) is min^{-1}) associated with the de-hydrochlorination of Fe_2O_3-PVC (third stage in Figure 2 (C)).

The apparent activation energy changes greatly with conversion starting at 112.9 kJ/mol at a conversion of 0.1 and reaching a maximum of 311.5 kJ/mol (Friedman) at a conversion of 0.5. It is believed that the capturing of emitted HCl by the Fe_3O_4 formed from the reduction of Fe_2O_3 can affect the value of the activation energy. This is because HCl was reported to catalyse the

de-hydrochlorination [35]. This can be confirmed by the prominent XRD peaks of $FeCl_2$ and $FeCl_2.2H_2O$ seen in Figure 6. The apparent reaction model describing Fe_2O_3-PVC de-hydrochlorination is best described by mechanism F_3 between $0.4 < \alpha < 0.9$ except for $\alpha = 0.7$ (A_4 model had a better fit). Different reaction models described the degradation below $\alpha = 0.4$.

To compare the effect of Fe_3O_4 and Fe_2O_3 on the de-hydrochlorination rate of PVC, the effect of the frequency factors shown in Figures 9, 11 and 13 must also be taken into account. This is achieved by comparing the rate and the rate constant for each system against the conversion at fixed temperatures of 250 and 300 °C (Figure 14).

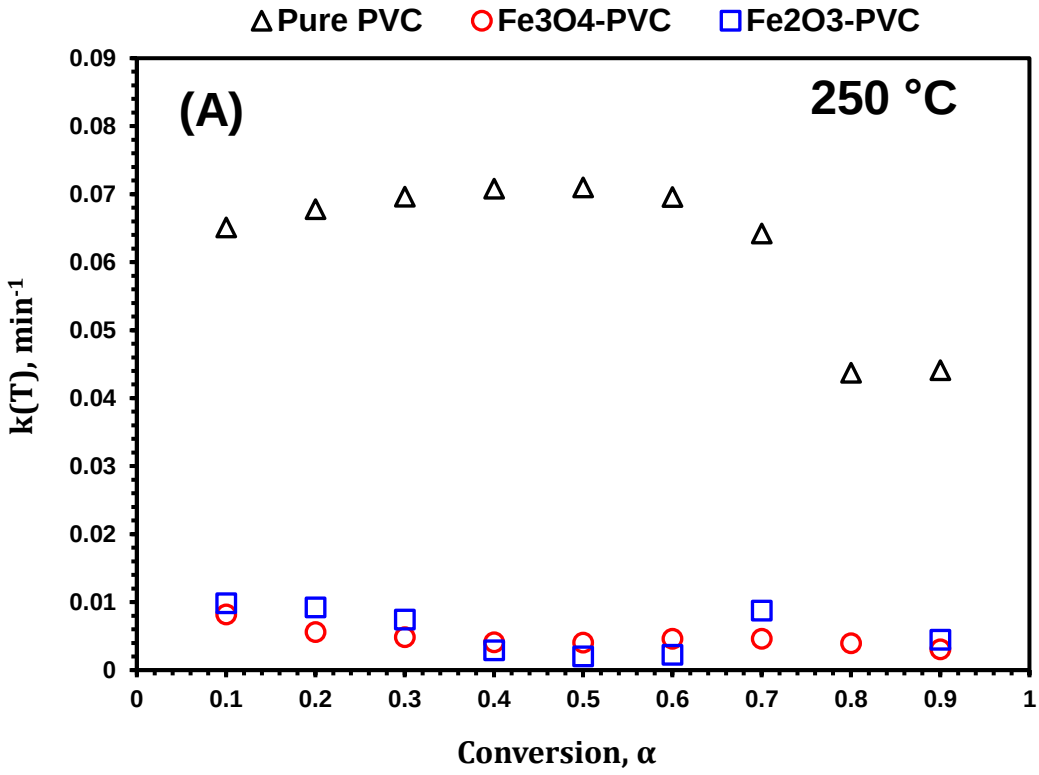

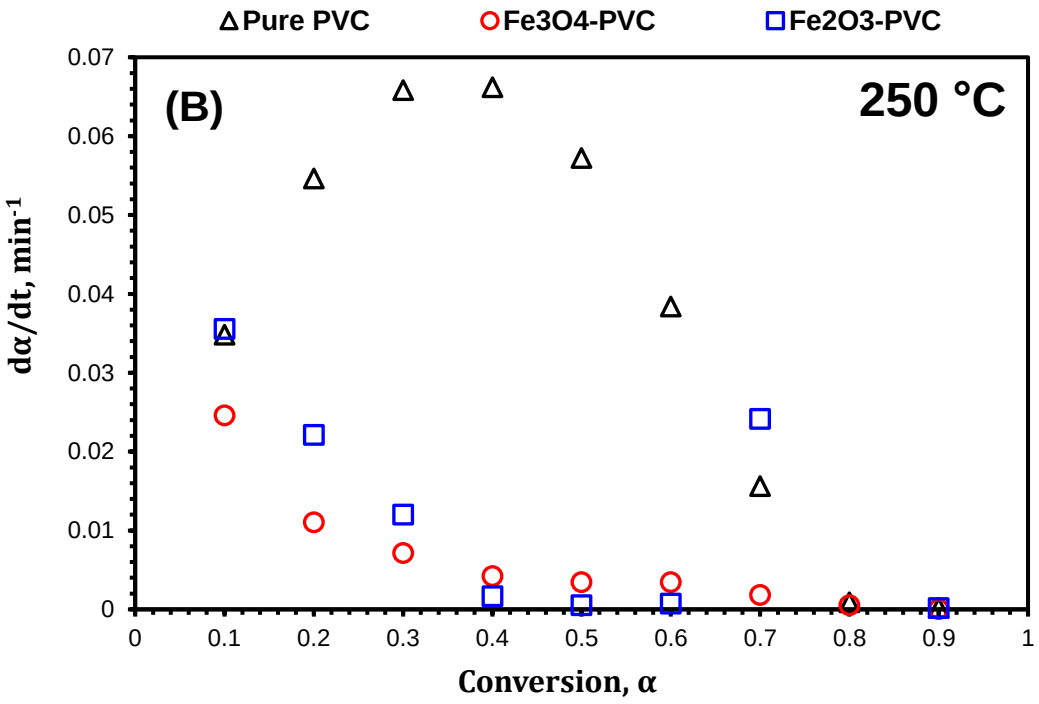
Pure PVC
Fe3O4-PVC
Fe2O3-PVC
(B)
250 °C
dα/dt, min-1
Conversion, α

75

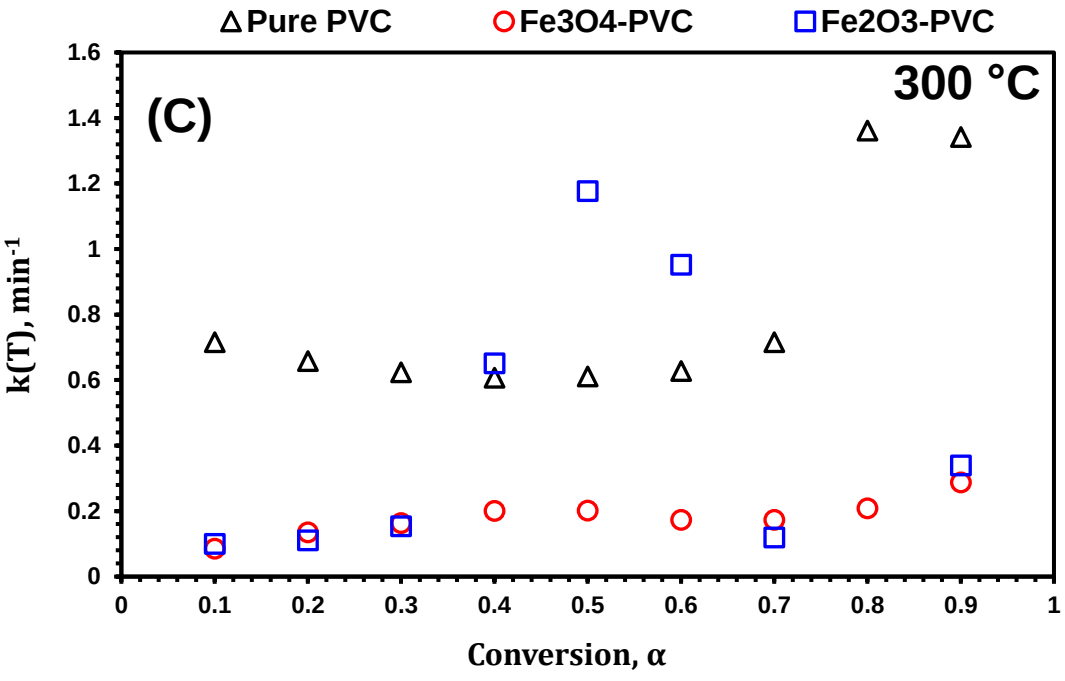
Pure PVC
Fe3O4-PVC
Fe2O3-PVC
(C)
300 °C
k(T), min-1
Conversion, α

76

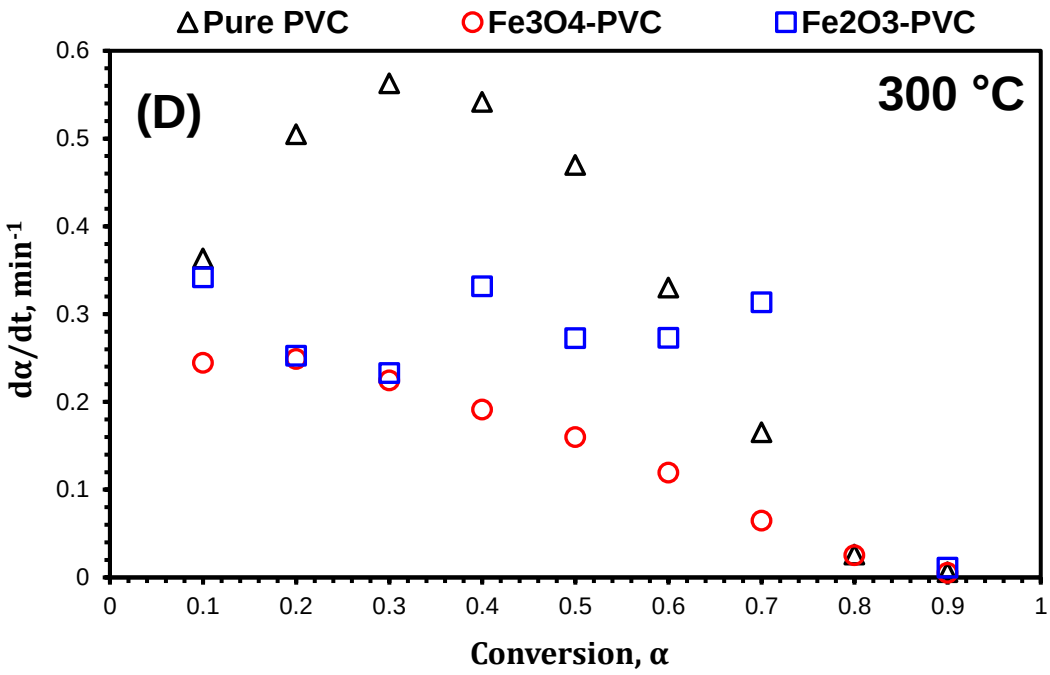

Figure 14: de-hydrochlorination rate (B) and (D) and rate constant (A) and (C) calculated using data from Freidman model of pure PVC, Fe_3O_4-PVC (31.6 wt% Fe_3O_4), and Fe_2O_3-PVC (29.9 wt% Fe_2O_3) at different conversion levels and at constant temperatures of 250 and 300 °C.

It is clear that the addition of both Fe_3O_4 and Fe_2O_3 to PVC yields a drop in the rate of mass loss associated with the de-hydrochlorination stage as shown in Figures 14 (B) and (D). Since the decomposition of Fe_3O_4-PVC and Fe_2O_3-PVC mixtures exhibit high activation energies, they can be described as strongly temperature dependent. Hence, it can be seen that the difference in the degradation rate between pure PVC and Fe_3O_4-PVC/Fe_2O_3-PVC becomes smaller when the temperature is increased from 250 to 300 °C. This is evident from the behaviour of the rate constant presented in Figures 14 (A) and (C), where, for instance, at a conversion of 0.5, the rate constant for pure PVC degradation is 17.8 and 35.5 times that of Fe_3O_4-PVC and Fe_2O_3-PVC at 250 °C while it is 3.0 and 0.52 times the rate constant of Fe_3O_4-PVC and Fe_2O_3-PVC at 300 °C. This means, at high temperatures, the activation energy barrier is overcome, and the high frequency factor associated with the de-hydrochlorination of Fe_3O_4-PVC/Fe_2O_3-PVC compensates for their high energy barrier leading to higher reaction rates.

The reliability of the extracted kinetic data can be confirmed from comparing the mass loss rates calculated from the kinetic parameters extracted here with the experimental rates (Figure

15). An excellent agreement between experimental and model generated rates of de-hydrochlorination can be seen in Figure 15 for the three different systems (PVC, Fe_3O_4-PVC, and Fe_2O_3-PVC). Presenting the data in Figure 15 at different heating rates was done to confirm that the generated kinetic parameters from Friedman model can produce correct mass loss rate values at different temperatures. The results in Figure 15 suggest the reliability of the kinetic parameters at temperatures in the vicinity of the temperatures used to generate these profiles.

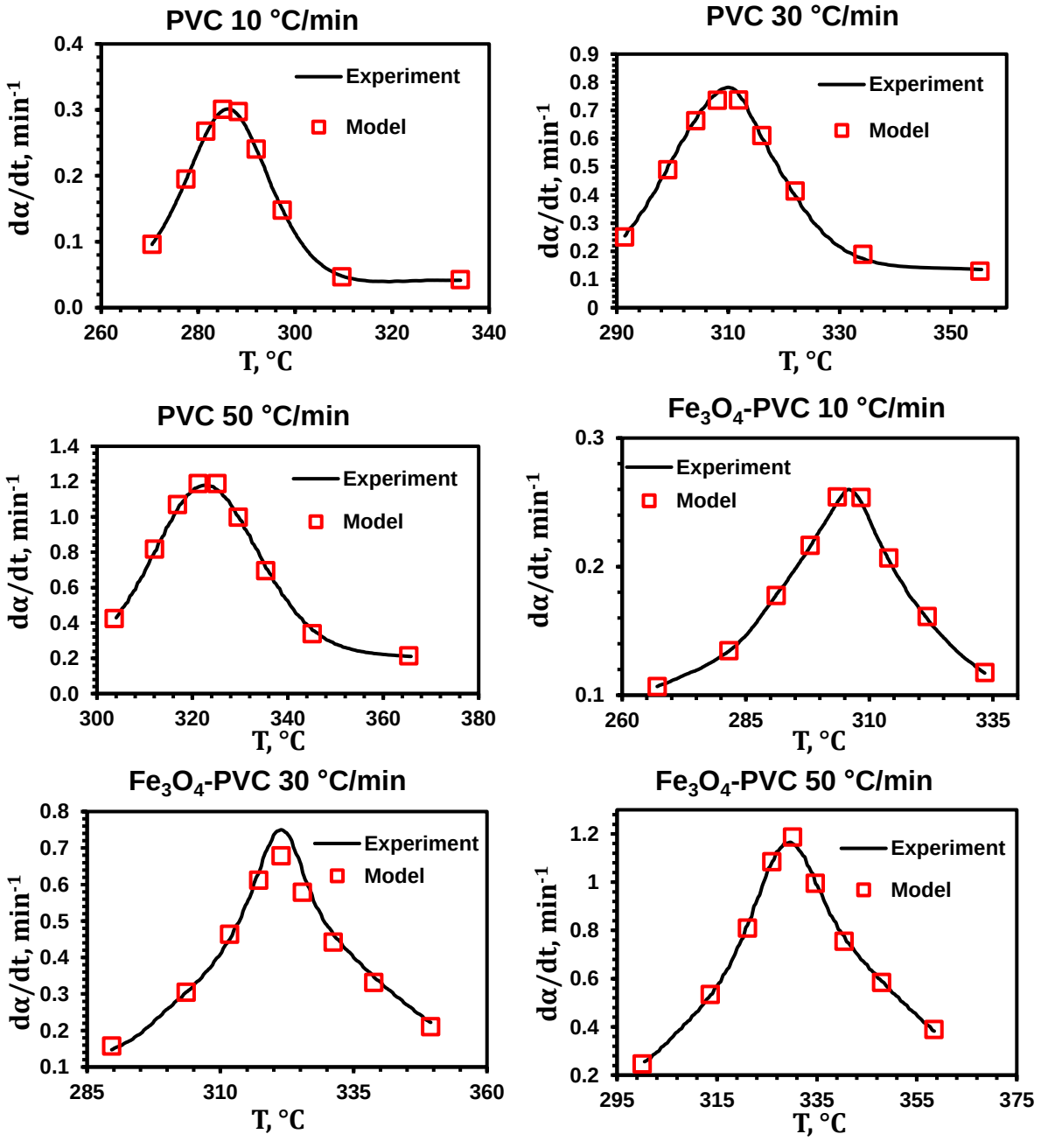

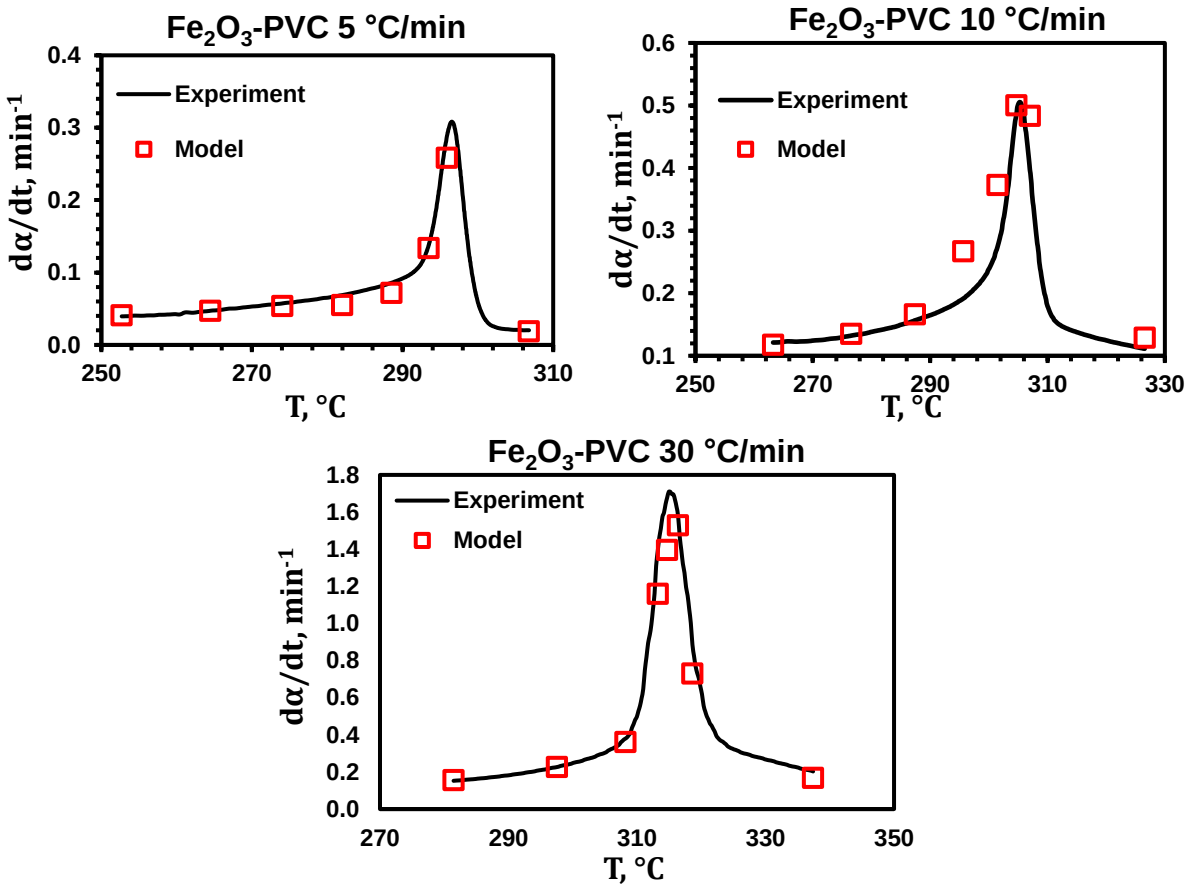

Figure 15: de-hydrochlorination experimental rates against the rate calculated using kinetic data obtained from Friedman method for Pure PVC, Fe_3O_4-PVC, and Fe_2O_3-PVC at different heating rates.

The thermo-kinetic study presented in this work provide answers to essential questions regarding the effect of individual components of EAFD (Fe_3O_4 and Fe_2O_3) on the decomposition kinetics of PVC. This work is part of an ongoing study addressing the effect of each EAFD component on the degradation kinetics of PVC. Previously, the effect of ZnO and $ZnFe_2O_4$ on the degradation kinetics of PVC was considered [34, 36]. The overall objective is to establish a kinetic database based on which the reaction rates of PVC with EAFD from different plants/countries with different mineral composition can be predicted. The utilisation of the kinetic parameters presented here contributes greatly to the optimisation of the co-thermal treatment of EAFD-PVC mixtures by selecting the optimal reaction temperatures which should make a balance between reaction times and process economics. Further investigation needs to be performed on other EAFD constituents such as litharge/massicot (PbO) under pyrolytic conditions. At the end, all these studies combined should be collected in

one work and a simulation study based on these parameters should be made to predict the kinetic effect of EAFD with different chemistries on PVC degradation.

5. Conclusions

This work reports the thermo-kinetic behaviour of PVC in the presence of Fe_3O_4 (a major EAFD component) and Fe_2O_3. The chlorination of Fe_3O_4 at a temperature of 400 °C was confirmed by the XRD peaks of $FeCl_2.2H_2O$. Despite the fact that the chlorination of Fe_2O_3 by HCl is thermodynamically unfavourable, the presence of reducing agents (such as H_2) during the de-hydrochlorination transformed Fe_2O_3 into Fe_3O_4 which was then chlorinated into $FeCl_2$ which was evaporated when the temperature was increased up to 850 °C. Performing the pyrolysis of Fe_3O_4-PVC and Fe_2O_3-PVC at a temperature of 850 °C yielded elemental iron α-Fe, suggesting that PVC can also be used as a reducing agent aside to being a source for chlorination.

The thermogravimetric scans under pyrolytic conditions (N_2) were used along with the model-free methods of Friedman and Ortega to calculate the kinetic parameters associated with the de-hydrochlorination of pure PVC and its mixtures with Fe_3O_4 and Fe_2O_3. The extracted kinetic data suggests that both Fe_3O_4 and Fe_2O_3 have an inhibiting effect on the de-hydrochlorination of PVC resulting in a significant increase in the value of the apparent activation energy along with an insufficient increase in the frequency factor. This, in turn, results in lower values of the overall rate of degradation for these mixtures compared to pure PVC at the common PVC pyrolysis temperatures of 250 and 300 °C.

6. Acknowledgment

The authors would like to thank Sabrin Samad from the Nanoscale and Microscale Research Centre (nmRC) at the University of Nottingham for helping with the SEM analysis.

References

[1] H. Zhu, X. Jiang, J. Yan, Y. Chi, K. Cen, TG-FTIR analysis of PVC thermal degradation and HCl removal, Journal of analytical and applied pyrolysis, 82 (2008) 1-9.

[2] W.S. Association, Steel Facts. A collection of amazing facts about steel. Worldsteel, in, 2018.

[3] M. Sebag, C. Korzenowski, A. Bernardes, A. Vilela, Evaluation of environmental compatibility of EAFD using different leaching standards, Journal of hazardous materials, 166 (2009) 670-675.

[4] M. Al-Harahsheh, J. Al-Nu'airat, A. Al-Otoom, H. Al-jabali, M. Al-zoubi, Treatments of electric arc furnace dust and halogenated plastic wastes: A review, Journal of Environmental Chemical Engineering, 7 (2018) 102856.

[5] M. Sadat-Shojai, G.-R. Bakhshandeh, Recycling of PVC wastes, Polymer Degradation and Stability, 96 (2011) 404-415.

[6] Y. Zhou, N. Yang, S. Hu, Industrial metabolism of PVC in China: A dynamic material flow analysis, Resources, Conservation and Recycling, 73 (2013) 33-40.

[7] I. Mersiowsky, R. Stegmann, J. Ejlertsson, Long term behaviour of poly (vinyl chloride) products under soil buried and landfill conditions, Plastics, rubber and composites, 28 (1999) 321-326.

[8] S. Kim, Pyrolysis kinetics of waste PVC pipe, Waste management, 21 (2001) 609-616.

[9] Y. Masuda, T. Uda, O. Terakado, M. Hirasawa, Pyrolysis study of poly (vinyl chloride)–metal oxide mixtures: quantitative product analysis and the chlorine fixing ability of metal oxides, Journal of Analytical and Applied Pyrolysis, 77 (2006) 159-168.

[10] M. Al-harahsheh, S. Kingman, L. Al-Makhadmah, I.E. Hamilton, Microwave treatment of electric arc furnace dust with PVC: Dielectric characterization and pyrolysis-leaching, Journal of Hazardous Materials, 274 (2014) 87-97.

[11] M. Al-Harahsheh, A. Al-Otoom, L. Al-Makhadmah, I.E. Hamilton, S. Kingman, S. Al-Asheh, M. Hararah, Pyrolysis of poly(vinyl chloride) and—electric arc furnacedust mixtures, Journal of Hazardous Materials, 299 (2015) 425-436.

[12] M. Al-Harahsheh, Thermodynamic Analysis on the Thermal Treatment of Electric Arc Furnace Dust-PVC Blends, Arabian Journal for Science and Engineering, 43 (2017) 1-13.

[13] G.-S. Lee, Y.J. Song, Recycling EAF dust by heat treatment with PVC, Minerals engineering, 20 (2007) 739-746.

[14] M. Al-Harahsheh, Y. Orabi, S. Al-Asheh, Comparative study on the pyrolysis and leachability of washed/unwashed electric arc furnace dust-PVC mixtures and their residues, Journal of Environmental Chemical Engineering, (2021) 105410.

[15] M. Al-Harahsheh, S. Altarawneh, M. Al-Omari, M. Altarawneh, S. Kingman, C. Dodds, Leaching behavior of zinc and lead from electric arc furnace dust–Poly (vinyl) chloride residues after oxidative thermal treatment, Journal of Cleaner Production, 328 (2021) 129622.

[16] M. Al-Harahsheh, M. Aljarrah, A. Al-Otoom, M. Altarawneh, S. Kingman, Pyrolysis kinetics of tetrabromobisphenol a (TBBPA) and electric arc furnace dust mixtures, Thermochimica Acta, 660 (2018) 61-69.

[17] J. Šesták, G. Berggren, Study of the kinetics of the mechanism of solid-state reactions at increasing temperatures, Thermochimica Acta, 3 (1971) 1-12.

[18] S. Vyazovkin, A.K. Burnham, J.M. Criado, L.A. Pérez-Maqueda, C. Popescu, N. Sbirrazzuoli, ICTAC Kinetics Committee recommendations for performing kinetic computations on thermal analysis data, Thermochimica acta, 520 (2011) 1-19.

[19] H.L. Friedman, Kinetics of thermal degradation of char-forming plastics from thermogravimetry. Application to a phenolic plastic, in: Journal of Polymer Science Part C: Polymer Symposia, Wiley Online Library, 6 1964, pp. 183-195.

[20] A. Ortega, A simple and precise linear integral method for isoconversional data, Thermochimica Acta, 474 (2008) 81-86.
[21] S. Vyazovkin, Determining Preexponential Factor in Model-Free Kinetic Methods: How and Why?, Molecules, 26 (2021) 3077.
[22] V. Georgieva, D. Zvezdova, L. Vlaev, Non-isothermal kinetics of thermal degradation of chitin, Journal of thermal analysis and calorimetry, 111 (2013) 763-771.
[23] A. Marcilla, M. Beltrán, Thermogravimetric kinetic study of poly(vinyl chloride) pyrolysis, Polymer Degradation and Stability, 48 (1995) 219-229.
[24] L. Ye, T. Li, L. Hong, Co-pyrolysis of Fe3O4-poly (vinyl chloride)(PVC) mixtures: Mitigation of chlorine emissions during PVC recycling, Waste Management, 126 (2021) 832-842.
[25] J. Yu, L. Sun, C. Ma, Y. Qiao, H. Yao, Thermal degradation of PVC: A review, Waste Management, 48 (2016) 300-314.
[26] A. Ballistreri, S. Foti, P. Maravigna, G. Montaudo, E. Scamporrino, Effect of metal oxides on the evolution of aromatic hydrocarbons in the thermal decomposition of PVC, Journal of Polymer Science: Polymer Chemistry Edition, 18 (1980) 3101-3110.
[27] S.B. Kanungo, Kinetics of thermal dehydration and decomposition of hydrated chlorides of 3d transition metals (Mn-Cu series). Part-II. Dehydration of FeCl2.4H2O, Journal of India Chemical Society, 81 (2004) 750-756.
[28] N. Louvain, A. Fakhry, P. Bonnet, M. El-Ghozzi, K. Guérin, M.-T. Sougrati, J.-C. Jumas, P. Willmann, One-shot versus stepwise gas–solid synthesis of iron trifluoride: investigation of pure molecular F 2 fluorination of chloride precursors, CrystEngComm, 15 (2013) 3664-3671.
[29] J. Zieliński, I. Zglinicka, L. Znak, Z. Kaszkur, Reduction of Fe2O3 with hydrogen, Applied Catalysis A: General, 381 (2010) 191-196.
[30] A. Pineau, N. Kanari, I. Gaballah, Kinetics of reduction of iron oxides by H2: Part II. Low temperature reduction of magnetite, Thermochimica Acta, 456 (2007) 75-88.
[31] B. Zhang, X.-Y. Yan, K. Shibata, T. Uda, M. Tada, M. Hirasawa, Thermogravimetric-mass spectrometric analysis of the reactions between oxide (ZnO, Fe2O3 or ZnFe2O4) and polyvinyl chloride under inert atmosphere, Materials Transactions, JIM, 41 (2000) 1342-1350.
[32] B. Morosin, E.J. Graeber, Crystal structures of manganese (II) and iron (II) chloride dihydrate, The Journal of Chemical Physics, 42 (1965) 898-901.
[33] K. Momma, F. Izumi, VESTA: a three-dimensional visualization system for electronic and structural analysis, Journal of Applied crystallography, 41 (2008) 653-658.
[34] S. Altarawneh, M. Al-Harahsheh, C. Dodds, A. Buttress, S. Kingman, Thermal degradation kinetics of polyvinyl chloride in presence of zinc oxide, Thermochimica Acta, 707 (2021) 179105.
[35] W.H. Starnes, X. Ge, Mechanism of autocatalysis in the thermal dehydrochlorination of poly (vinyl chloride), Macromolecules, 37 (2004) 352-359.
[36] S. Altarawneh, M. Al-Harahsheh, C. Dodds, A. Buttress, S. Kingman, Thermodynamic, pyrolytic, and kinetic investigation on the thermal decomposition of polyvinyl chloride in the presence of franklinite, Process Safety and Environmental Protection, 168 (2022) 558-569.